Progress in Energy

TOPICAL REVIEW

Balancing selectivity and permeability in nanofluidic membranes for osmotic power generation

To cite this article: Han Qian *et al* 2025 *Prog. Energy* **7** 042001

IOP Publishing Prog. Energy 7 (2025) 042001 https://doi.org/10.1088/2516-1083/ae0117

Progress in Energy

RECEIVED
31 December 2024

REVISED
28 February 2025

ACCEPTED FOR PUBLICATION
29 August 2025

PUBLISHED
16 September 2025

TOPICAL REVIEW

Balancing selectivity and permeability in nanofluidic membranes for osmotic power generation

Han Qian[1,2], **Puguang Peng**[1,2], **Yanhui Liu**[1,2], **Zhong Lin Wang**[1,3,*] and **Di Wei**[1,4,*]

[1] Beijing Institute of Nanoenergy and Nanosystems, Chinese Academy of Sciences, Beijing 101400, People's Republic of China
[2] School of Nanoscience and Engineering, University of Chinese Academy of Sciences, Beijing 100049, People's Republic of China
[3] Beijing Key Laboratory of Micro-Nano Energy and Sensor, Center for High-Entropy Energy and Systems, Beijing Institute of Nanoenergy and Nanosystems, Chinese Academy of Sciences, Beijing 101400, People's Republic of China
[4] Centre for Photonic Devices and Sensors, University of Cambridge, 9 JJ Thomson Avenue, Cambridge CB3 0FA, United Kingdom
[*] Authors to whom any correspondence should be addressed.

E-mail: zhong.wang@mse.gatech.edu and dw344@cam.ac.uk

Keywords: selectivity, permeability, osmotic power generation, nanofluidic membrane, nanofluidic reverse electrodialysis

Abstract

Osmotic energy, also known as 'blue energy', harnesses the salinity gradient between seawater and freshwater, providing a vast, renewable, and environmentally friendly energy source. The efficiency of osmotic power generation is fundamentally dependent on the performance of ion-exchange membranes, where a critical trade-off exists between ion selectivity and ion permeability, which determine the voltage and current respectively. Recent advances in nanofluidic reverse electrodialysis (NRED) have leveraged nanoconfined spaces and innovative membrane design to significantly minimize resistance and promote energy conversion. In this review, we systematically explore the ion transport mechanisms in nanoconfined spaces, analyze state-of-the-art membrane optimization parameters to balance the selectivity-permeability trade-off. Finally, we discuss current challenges and prospective future directions for membrane innovation in NRED-based osmotic power generation systems, with the ultimate target of facilitating the practical realization of high-performance, commercially viable osmotic power generation.

1. Introduction

The escalating global energy demand, coupled with the environmental challenges posed by fossil fuel consumption, necessitates the exploration of renewable energy sources such as solar, wind, and ocean energy [1, 2]. Among these, osmotic energy, also known as 'blue energy', is derived from the salinity gradients between freshwater and seawater, offering a sustainable and abundant energy resource [3, 4]. It has vast global energy reserves (approximately 2 TW) with minimal environmental pollution and carbon dioxide emissions [5]. One of the most promising technologies for harnessing osmotic power is reverse electrodialysis (RED). The RED operates by placing alternating cation-exchange membrane and anion-exchange membrane between solutions with different salinity gradients, facilitating ion transport that generates electrical power [3, 6]. The efficiency of RED systems is critically dependent on the performance of the ion-exchange membranes (IEMs) [7, 8]. Key membrane properties include selectivity (the ability to preferentially transport specific ions) and permeability (the capacity to allow ions to pass through under salinity gradients), which together determine the overall power output and conversion efficiency of the system [9]. Therefore, advancements in membrane technology are pivotal in optimizing RED processes for effective osmotic power generation and meet the commercial benchmark (over 5 W m^{-2}) [10].

In biological systems, ion channels and pumps play an essential role in the precise and efficient transport of ions, enabling a wide range of life-sustaining processes [11, 12]. These channels exhibit both high selectivity and permeability, allowing organisms to regulate various physiological functions [13, 14]. For example, the potassium channel, whose structure was elucidated by MacKinnon in 1998, demonstrates how biological ion channels selectively allow potassium ions to pass while excluding others, thereby maintaining cellular homeostasis and conducting action potentials [15] (figure 1). However, in biomimetic systems, such

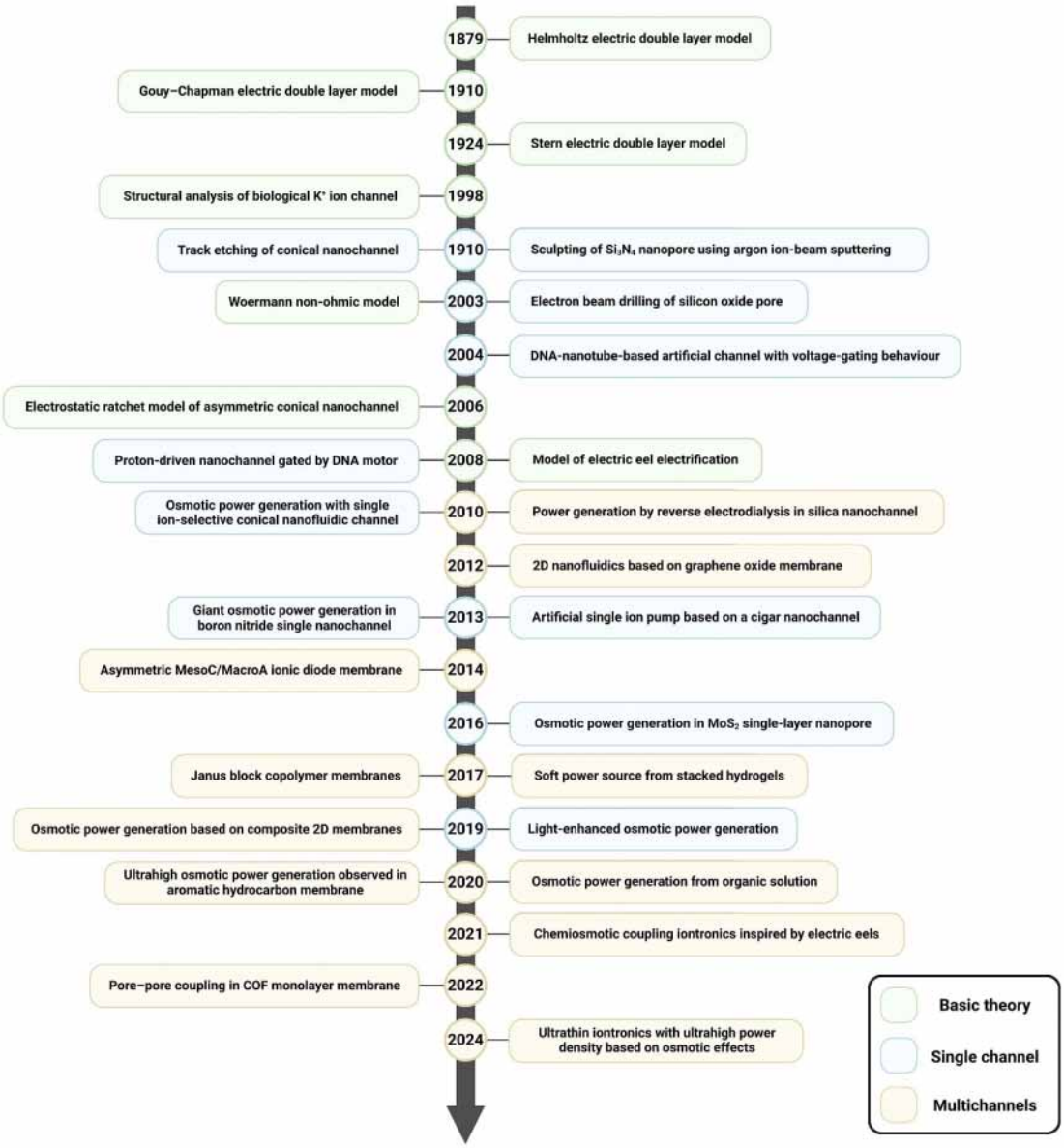

Figure 1. Theoretical and practical milestones in nanofluidic reverse electrodialysis (NRED). The timeline shows advances in basic theory, single channel platform, and multichannel membrane systems, including fundamental electrochemistry and bioinspired nanofluidics.

as RED processes for osmotic power generation, traditional IEMs face significant trade-off between selectivity and permeability [16–18]. While increased selectivity ensures the preferential transport of specific ions, it often reduces the membrane's permeability, which limits the rate of ion flow and the power output [9, 19, 20]. Conversely, enhancing permeability may compromise selectivity, leading to inefficiencies in the salinity gradient that powers RED systems [9, 21, 22]. To address these limitations, researchers have turned to nanofluidic systems, nanofluidic REDs (NRED), a promising development in osmotic power generation [7, 23]. Nanofluidics is the study of transport of fluids within nanoconfined channels, where intermolecular forces like van der Waals interactions, electrostatic forces, and hydration become dominant [23–26]. These forces, operating at the nanoscale or sub-nanoscale spaces, enable highly efficient and selective ion transport, mimicking the behavior of biological ion channels [27, 28]. The development process of nanofluidics is shown in figure 1.

As an advanced RED technology, NRED replaces conventional IEMs with nanochannels made from materials like graphene oxide (GO) (figure 1). Unlike traditional IEMs, NRED systems take advantage of the unique ion transport dynamics within nanoconfined channels, enabling both enhanced ion selectivity and increased ion flux [7, 16, 29]. Research indicates that NRED systems can achieve power densities several orders of magnitude higher than traditional RED systems, owing to their enhanced ion flux and reduced resistance [10]. This positions NRED as a highly promising candidate for large-scale osmotic power

generation applications [30]. In the past two decades, NRED has evolved from theoretical predictions to the practical realization of solid-state nanofluidic systems for efficient energy conversion due to advancements in nanotechnology and fabrication techniques [7, 30, 31]. Early breakthroughs in nanofabrication, such as ion-beam sputtering and electron-beam etching, enabled the creation of nanochannels and/or nanopores in materials like Si_3N_4 and SiO_2 [32, 33]. These structures mimic biological ion channels, providing insights into ion transport mechanisms and improving osmotic power generation performance. Despite advancements, there are also challenges like scalability, membrane fouling, and long-term stability of NRED systems. Resolving these challenges is essential for large-scale implementation and maximizing energy efficiency in sustainable energy harvesting [5, 22, 34, 35].

Based on the above challenges, the aim of this review is to give an overview of the latest advancements in NRED systems for osmotic power generation to overcome the trade-off between membrane selectivity and permeability from mechanisms to design strategies. We begin by introducing the highly integrated selectivity and permeability of ion channels in nature, which provide a biomimetic inspiration for constructing biomimetic nanochannels. Subsequently, grounded in biomimetic systems' trade-off between selectivity and permeability, we emphatically elucidated how the mechanisms by which the unique ion dynamics in nanoconfined channels enhance both selectivity and permeability. Furthermore, the discussion extends to the impact of structural and functional parameters, such as pore size, charge density, membrane thickness, ion transport pathways, structure design, and the introduction of external fields—on overcoming the trade-off, offering a comprehensive analysis of prior attempts to optimize NRED systems. Finally, we explore the challenges and opportunities associated with NRED systems for osmotic power generation, aspiring to provide judicious guidance for future designs that address the selectivity-permeability trade-off.

2. Ion transport in biological and biomimetic systems

2.1. Selectivity-permeability combinations in biological systems

Ion transport is a ubiquitous phenomenon in nature, primarily facilitated by transmembrane proteins [11, 36]. These proteins are fundamental to vital life activities such as information transmission and energy conversion [11, 14, 15]. In neurons, the generation and propagation of action potentials depend on the movement of sodium (Na^+) and potassium (K^+) ions [37]. Upon stimulation, voltage-gated sodium channels open, allowing Na^+ to flow into the cell, leading to membrane depolarization [38]. Subsequently, potassium channels open, permitting K^+ to exit the cell, restoring the membrane potential to its resting state [39, 40] (figure 2(a)). During synaptic transmission, when an action potential reaches the synaptic terminal, it triggers the opening of voltage-gated calcium channels, resulting in an influx of calcium ions (Ca^{2+}) [41, 42]. The increase in intracellular Ca^{2+} concentration prompts synaptic vesicles to fuse with the presynaptic membrane, releasing neurotransmitters into the synaptic cleft and thereby transmitting signals between neurons [43, 44] (figure 2(a)). In addition to information transfer, precise and efficient ion transport plays an equally important role in energy conversion [11]. In mitochondria, protons (H^+) are pumped into the intermembrane space via the electron transport chain, creating a H^+ gradient. This chemiosmotic coupling drives ATP synthase to produce ATP, supplying energy for various cellular activities [45, 46] (figure 2(b)). These ion transport proteins exhibit remarkable ion selectivity and permeability. For instance, sodium channels can select Na^+ over K^+ by a factor of up to 100, with a Na^+ permeability of approximately 0.02 kmol s^{-1} m^{-2} [47–49]. The high efficiency of these biological systems offers valuable insights for designing biomimetic structures, inspiring the development of high-performance biomimetic IEMs for NRED systems and osmotic power generation.

2.2. Ion selectivity-permeability trade-off in biomimetic NRED systems

2.2.1. Generation of osmotic power

Osmotic power generation relies on two fundamental conditions: the existence of solutions with different salinity gradients and the disparity in diffusion rates of anions and cations. Driven by the chemical potential gradient, ions move from a high-salinity region to a low-salinity region [20]. To differentiate the transport rates of anions and cations, IEMs were introduced between the solutions. The nanochannels of the membrane, characterized by surface charges, enable selective transport of either cations or anions based on their charge. To maintain electroneutrality, redox reactions occur at the electrodes, resulting in a net ion flux, termed the osmotic current [50].

The theoretical maximum amount of osmotic energy dG can be described by the following equation:

$$\mathrm{d}G = -\frac{RT}{F}\ln\frac{\tau_{\mathrm{H}}}{\tau_{\mathrm{L}}}\left(|I_+| + |I_-|\right)\mathrm{d}t \tag{1}$$

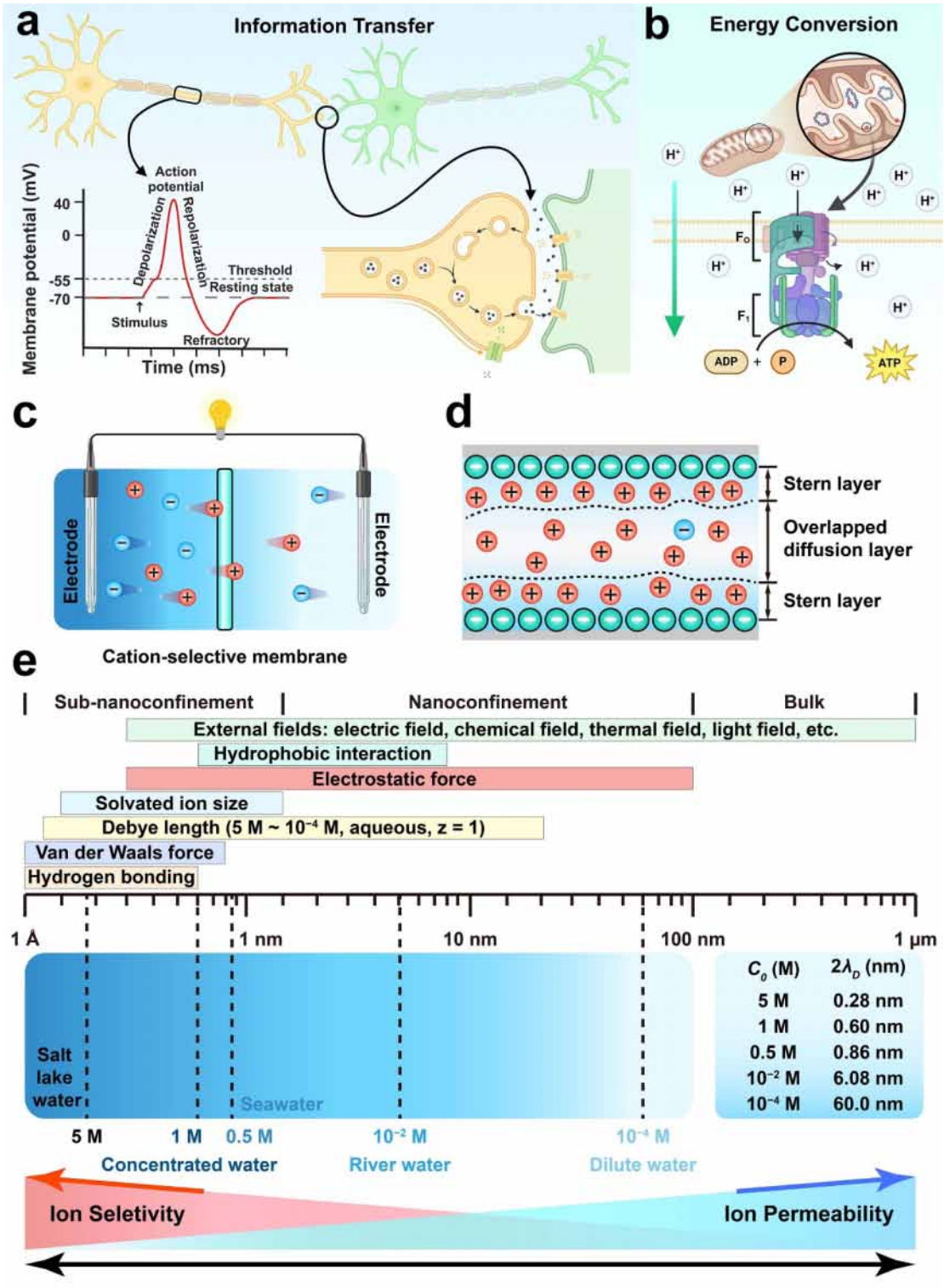

Figure 2. Ion transport in biological and biomimetic systems. (a) Schematic of information transfer process in neurons. (b) Schematic of energy conversion process in mitochondrion. (c) Schematics of the osmotic power generation devices based on ion-exchange membranes (IEMs). (d) Schematic of ion selectivity in a surface-charged nanochannel. (e) A trade-off between pore-size-dependent ion selectivity and ion permeability. The critical values of λ_D at specific concentrations (C_0) in typical saline waters, as well as ion interactions in various confined systems, are summarized.

where R is the universal gas constant (8.314 J mol^{-1} K^{-1}), T is the absolute temperature (K), F represents the Faraday constant (96485.3 C mol^{-1}), τ_H and τ_L denote the activities of the saline solutions on the high- and low-salinity sides, respectively. I_+ and I_- represent the diffusion currents of cations and anions [20, 51].

When solutions with different salinity gradients mix, a portion of the Gibbs free energy is converted into electric work (dW), which can be calculated as:

$$dW = \frac{RT}{F}\ln\frac{\tau_H}{\tau_L}\frac{(|I_+| - |I_-|)^2}{(|I_+| + |I_-|)}dt. \tag{2}$$

The efficiency of energy conversion (φ) could be expressed by the following equation:

$$\varphi = \left|\frac{dW}{dG}\right| = \frac{(|I_+| - |I_-|)^2}{(|I_+| + |I_-|)^2}. \tag{3}$$

From these equations, it is evident that a net current arises only if the diffusion rates or directions of anions and cations differ significantly. The net current diminishes when these mobilities are comparable, emphasizing the importance of enhancing mobility differences to maximize osmotic power generation [52].

The maximum power density (P_{max}), can be determined by following equation:

$$P_{max} = \frac{E_{osm}^2}{4R_M}. \tag{4}$$

Here, E_{osm} is the osmotic potential, and R_M represents the internal resistance of the membrane. E_{osm}, equivalent to the Nernst potential across the membrane, which can be defined by the following equation:

$$E_{osm} = S\frac{RT}{zF}\ln\frac{c_H}{c_L} \tag{5}$$

where S is the membrane selectivity, z denotes valence charge, c_H and c_L are the electrolyte concentrations at the high- and low-concentration regions, respectively [53].

In devices, maximum power density (P_{max}) can also be evaluated by connecting an external resistance R_L, to the circuit. When R_M is nearly equal to R_L, P_{max} can be described by the following equation:

$$P_{max} = I_{osm}^2 R_L \tag{6}$$

where I_{osm} is the current corresponding to the matched load resistance [54].

2.2.2. Ion selectivity and permeability

As mentioned above, the function of the IEMs is to differentiate the transport rates of cations and anions. Ideally, these membranes allow only counter-ions to pass while completely excluding co-ions [9]. However, in practical transport processes, achieving perfect ion selectivity is challenging due to factors such as ion hydration, steric effects, and non-ideal interactions within the membrane's pores [21, 28]. In aqueous solutions, charged surfaces attract counter-ions through Coulombic forces, forming an electrical double layer (EDL) composed of a Stern layer (a layer of counter-ions near the solid surface) and a diffuse layer (extending from the Stern layer to bulk solution) [4, 55]. The ion selectivity of membranes primarily originates from the EDL formed within the charged pore with a diameter of D. In the EDL, the concentration of counter-ions is significantly higher than that of co-ions. c [56]. The Debye length inversely correlates with ionic concentration. When the channel radius approaches the Debye length, the EDL would be overlapped, and ion selectivity can be enhanced by excluding co-ions while permitting counter-ions [57].

When the $D \leqslant 2\lambda_D$, nanopores can exhibit significant ion selectivity [9]. Nanopores with larger values of the λ_D are particularly advantageous for membrane design, as they enhance ion selectivity and enable higher output voltages. Consequently, two primary strategies to improve the ion selectivity of membranes include reducing pore size or increasing surface charge density [4]. Figure 2(c) presents critical $2\lambda_D$ values of 0.28, 0.60, 0.86, 6.08, and 60 nm, corresponding to solution concentrations of 5, 1, 0.5, 10^{-2}, and 10^{-4} M in typical saline environments, respectively.

Membrane resistance, comprising Ohmic and non-Ohmic components, is another factor influencing ion transport across membranes [20, 58]. Ohmic resistance arises from ion transport through channels and can be expressed via the diffusion-osmotic velocity (V_{DO}):

$$V_{DO} \approx \frac{k_B T}{8\pi l_B \eta} \times \frac{\Delta \log c}{L} \tag{7}$$

where k_B, T, l_B, η, and L represent the Boltzmann constant, absolute temperature, Bjerrum length, water viscosity, and channel length, respectively [59, 60]. Δlogc is the logarithm of the concentration ratio [20]. For membranes with N pores, the osmotic current is:

$$I_{osm} \approx N \times 2\pi R_p \sum V_{DO} \tag{8}$$

where R_p is the pore radius and $\sum$ represents the surface charge density. Non-Ohmic resistance primarily arises from ion concentration polarization (ICP) at the interface between the membrane and solution, particularly on the low concentration side [61]. This occurs because the continuous ion diffusion from the high concentration region to the low concentration region reduces the salinity gradient between the inlet and outlet of the channels [62].

When an electric field is applied, the flow path of ions is determined by both the Poisson–Nernst–Planck equation. The Nernst–Planck equation describes the flux of each ionic species, incorporating the combined effects of diffusion, migration, and convection, thereby serving as the fundamental model for characterizing ion transport in electric fields. The ionic flux (J_i) is mathematically expressed as:

$$J_i = -D_i \nabla c_i - \frac{Z_i F}{RT} D_i c_i \nabla \Phi + c_i u \tag{9}$$

where D_i is the diffusion coefficient, c_i is the concentration, Z_i is the charge of the species i, F is Faraday's constant, Φ is the electrical potential, u is fluid velocity, R is gas constant, and T is absolute temperature. The hydrodynamic effects from the fluid flow are assumed to be negligible ($u = 0$). The relationship between the electric potential and ion concentrations is governed by the Poisson equation, which describes the electrostatic behavior of charge distributions. When coupled with the Nernst–Planck equation, it enables the simultaneous determination of the electric field and concentration field. The Poisson equation is formulated as:

$$\nabla^2 \Phi = -\frac{F}{\varepsilon} \sum_i Z_i c_i \tag{10}$$

where ε is permittivity of the fluid.

This coupled system of equations provides a comprehensive framework for analyzing ion transport dynamics in electric fields, incorporating both electrochemical and electrostatic interactions to accurately predict spatial and temporal variations in ion concentrations and potential distributions.

When the EDL overlapped effect becomes significant ($D \leqslant 2\lambda_D$), the pore predominantly facilitates counter-ion transport, revealing high ion selectivity. Minimizing pore size from the microscale to the sub-nanometer scale is expected to enhance ion selectivity notably, thereby improving output voltage. However, smaller pores also increase resistance, reducing ion transport efficiency and lowering the overall output current. To achieve efficient osmotic power generation, balancing ion selectivity and minimizing resistance is crucial. To maximize osmotic power, it is essential to address the trade-off between ion selectivity (voltage) and ion permeability (current) when designing membranes (figure 2(c)). There were three strategies, which have been attempted to balance this trade-off in state-of-the-art membranes for optimizing osmotic power and conversion efficiency [9]. The first strategy involves the use of nanoscale charged pores (2–50 nm), which offer a balance between ion selectivity and permeability. The second approach utilizes larger pores, typically at the submicron scale, with highly charged surfaces. These surfaces enhance both ion selectivity and permeability. The third strategy incorporates sub-nanometer pores, which can significantly improve membrane selectivity. During the implementation of these strategies, several parameters, including pore size, pore density, charge density, membrane thickness, ion transport pathway, structure design (e.g. Janus structure), and external fields, play a significant role. By optimizing these parameters, the trade-off between ion selectivity and permeability could be effectively balanced, enhancing the osmotic power and conversion efficiency of NRED.

3. Parameters for optimizing osmotic power generation of NRED systems

This section reviews the key parameters affecting the performance of IEMs in osmotic power generation. It encompasses both experimental findings and theoretical insights to provide a comprehensive understanding of fundamental principles and design strategies for optimizing osmotic power generation of NRED systems (table 1).

3.1. Pore size

Pore size is one of the most significant factors influencing the osmotic power conversion efficiency of IEMs [63, 64]. The decrease in the pore size can enhance the membrane's ion selectivity, resulting in higher osmotic voltage. However, this improvement comes at the cost of increased resistance, which reduces the osmotic current [65, 66]. In contrast, larger pores exhibit lower selectivity, leading to reduced osmotic potential and a corresponding decrease in osmotic current [66, 67]. The trade-off between ion selectivity (voltage) and ion permeability (current) creates a pore-size-dependent maximum in osmotic power density

Table 1. Summary of osmotic power generation in different membranes.

Membrane	Parameter	Condition	Power density	References
MoS_2	Pore size	1 M | 0.001 M KCl	10^6 W m^{-2}	[33]
BNNTs	Pore size	1 M | 0.001 M KCl	4 kW m^{-2}	[32]
PET	Pore size	1 M | 0.001 M KCl	1294 W m^{-2}	[68]
PET	Pore size	1 M | 0.001 M KCl	198 W m^{-2}	[70]
COF	Pore density	0.5 M | 0.01 M NaCl	200 W m^{-2}	[76]
2DNP	Pore density	1 M | 0.001 M KCl	2 kW m^{-2}	[77]
COF	Charge density	0.5 M | 0.01 M NaCl	51.9 W m^{-2}	[86]
MoS_2	Charge density	0.5 M | 0.01 M NaCl	6.7 W m^{-2}	[89]
MXene/Kevlar	Charge density	0.5 M | 0.01 M NaCl	4.1 W m^{-2}	[87]
O-MXene	Charge density	0.5 M | 0.01 M NaCl	21.7 W m^{-2}	[91]
MoS_2/BNC	Charge density	0.5 M | 0.01 M NaCl	73 W m^{-2}	[90]
MOF	Charge density	0.5 M | 0.01 M NaCl	10.8 W m^{-2}	[103]
MXene	Charge density	0.5 M | 0.01 M NaCl	9.68 W m^{-2}	[133]
GO	Charge density	0.5 M | 0.01 M NaCl	6.23 W m^{-2}	[134]
AAO	Membrane thickness	0.5 M | 0.01 M NaCl	5.1 W m^{-2}	[93]
SF	Membrane thickness	0.5 M | 0.01 M NaCl	4.06 W m^{-2}	[94]
MXene	Ion transport pathway	0.5 M | 0.01 M NaCl	9.47 W m^{-2}	[99]
GO	Ion transport pathway	1 M | 0.001 M KCl	13.15 W m^{-2}	[98]
GO	Ion transport pathway	0.5 M | 0.01 M NaCl	5.26 W m^{-2}	[96]
MXene	Ion transport pathway	0.5 M | 0.005 M KCl	17.5 W m^{-2}	[101]
COF/ANF	Ion transport pathway	0.5 M | 0.01 M NaCl	9.6 W m^{-2}	[100]
2DPI	Ion transport pathway	0.5 M | 0.01 M NaCl	53 W m^{-2}	[104]
MOF	Ion transport pathway	0.5 M | 0.01 M NaCl	10.08 W m^{-2}	[103]
COF	Ion transport pathway	0.5 M | 0.01 M NaCl	43.2 W m^{-2}	[102]
COF	Ion transport pathway	0.5 M | 0.01 M NaCl	14.1 W m^{-2}	[135]
PCM/NCM	Structural design	0.5 M | 0.01 M NaCl	8.6 W m^{-2}	[111]
COF	Structural design	0.5 M | 0.01 M NaCl	19.2 W m^{-2}	[108]
PES-Py/PAEK-HS	Structural design	5 M | 0.01 M NaCl	5.1 W m^{-2}	[113]
h-PEI	Structural design	5 M | 0.01 M NaCl	22.4 W m^{-2}	[110]
ZIF/PSS	Structural design	2 M LiCl | methanol	50.5 W m^{-2}	[112]
HOF/AAO	Structural design	5 M | 0.01 M NaCl	75.2 W m^{-2}	[114]
ACP	Structural design	0.5 M | 0.01 M KCl	11.7 W m^{-2}	[136]
PET/Hydrogel	Structural design	0.5 M | 0.01 M NaCl	1.92 W m^{-2}	[137]
GO/2DMC	Structural design	0.5 M | 0.01 M NaCl	6.41 W m^{-2}	[138]
MC/AAO/MS	Structural design	0.5 M | 0.01 M NaCl	5.37 W m^{-2}	[109]
PM/NM	Structural design	0.5 M | 0.01 M NaCl	16 W m^{-2}	[139]
ZIF/UiO	Structural design	0.5 M | 0.01 M NaCl	9.2 W m^{-2}	[107]
ZIF/UiO	Structural design	10 mM | 1 μM KCl	3.44 W m^{-2}	[140]
MXene/PBONF	Structural design	0.5 M | 0.01 M NaCl	15.7 W m^{-2}	[105]
GO/rGO	External fields	0.5 M | 0.01 M NaCl	15.9 kW m^{-2}	[118]
GO/rGO	External fields	0.5 M | 0.01 M NaCl	16.07 kW m^{-2}	[50]
COF	External fields	0.5 M | 0.01 M NaCl	231 W m^{-2}	[120]
COF	External fields	0.5 M | 0.01 M NaCl	247 W m^{-2}	[79]
COF	External fields	0.5 M | 0.01 M NaCl	210 W m^{-2}	[78]
MoS_2/BNC	External fields	0.5 M | 0.01 M NaCl	233 W m^{-2}	[90]
COF	External fields	0.5 M | 0.01 M NaCl	69.6 W m^{-2}	[121]
PESM/AAO	External fields	5 M | 0.01 M NaCl	70.4 W m^{-2}	[122]
Cu-TCPP	External fields	0.5 M | 0.01 M KCl	16.64 W m^{-2}	[123]
COF	External fields	0.5 M | 0.01 M NaCl	129 W m^{-2}	[124]
N-cage	External fields	0.5 M | 0.01 M KCl	5.8 W m^{-2}	[126]
COF	External fields	0.5 M | 0.01 M NaCl	155 W m^{-2}	[129]

[33]. For instance, Feng *et al* [33] verified this theory using a single-layer molybdenum disulfide (MoS_2) membrane with nanoscale charged pores (figure 3(a)). They employed atomic-scale electrochemical reaction technology and electron irradiation under transmission electron microscopy to fabricate nanoscale charged pores of varying sizes in the single-layer MoS_2 membrane (figure 3(b)). It was observed that when the pore size was approximately 10 nm, the maximum osmotic power output was achieved (figure 3(c)). If we have a single-layer MoS_2 membrane with a homogeneous pore size of 10 nm and a porosity of 30%, the estimated power density would reach 10^6 W m^{-2} with a 1 mM |1 M KCl salinity gradient. Similarly, Siria *et al* [32] used focused ion beam drilling on SiN membranes to create pores, into which multi-walled boron nitride

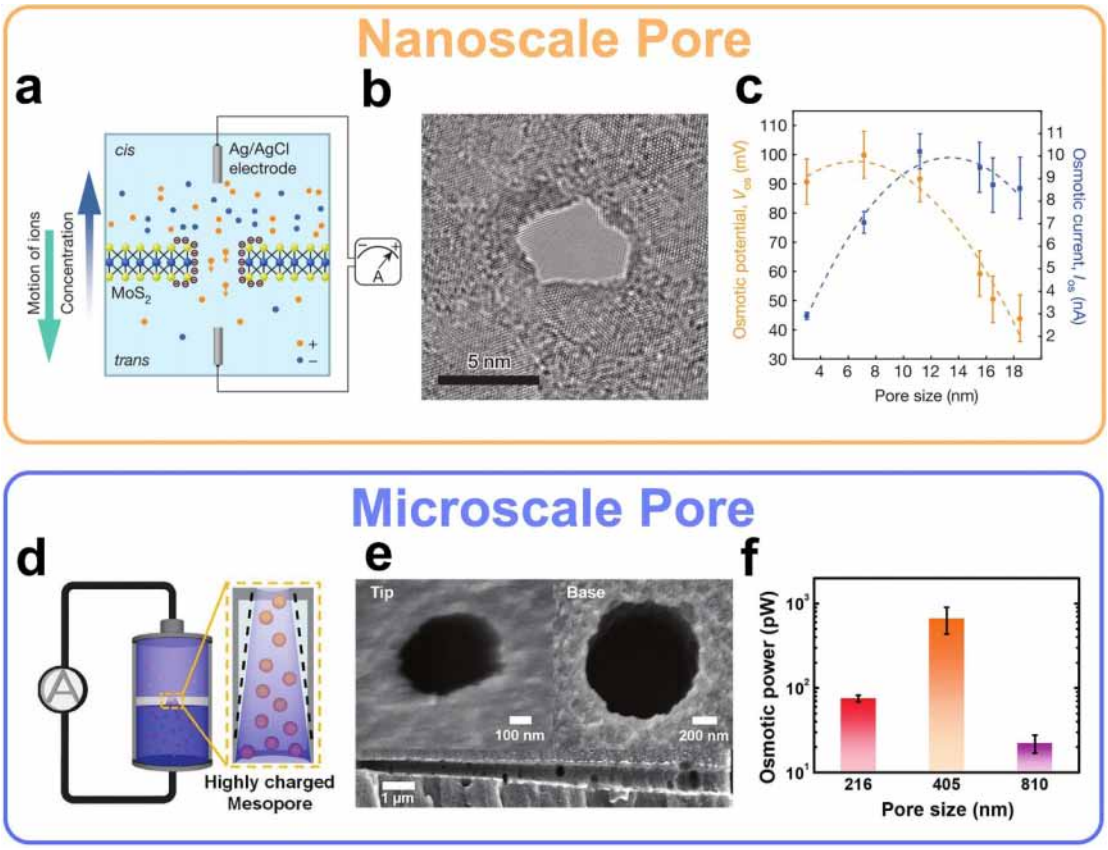

Figure 3. The effect of pore size on osmotic power conversion. (a) Single-layer MoS_2 nanoscale charged pores for osmotic power conversion. (b) The transmission electron microscopy (TEM) image of an MoS_2 nanoscale charged pore with a diameter of 5 nm. (c) Osmotic potential and current as a function of pore size. Reproduced from [33], with permission from Springer Nature. (d) Single-conical PET microscale charged pores with high surface charges density. (e) The scanning electron microscopy (SEM) images of the tip-face, base-face, and cross-section view of the microscale charged pore, indicating that the conical microscale charged pore was of 405 nm in tip diameter, 930 nm in base diameter, and 11.5 μm in pore length. (f) Osmotic powers generated by the single high surface charged conical microscale charged pores with various tip pore sizes ranging from 216 to 810 nm in 1000-fold salinity gradient. [68] John Wiley & Sons. (© 2020 Wiley-VCH GmbH).

nanotubes (BNNTs) were inserted. The pores were sealed using electron beam evaporation, resulting in single transmembrane BNNT membranes of various sizes. Under a 1000-fold KCl salinity gradient, the power density of a single BNNT reached 4 kW m^{-2} with a pore size of 40 nm, demonstrating efficient osmotic power generation potential of solid-state nanoscale charged pores. These studies, utilizing advanced micro-nanofabrication techniques, enabled the fabrication of nanoscale single-pore membranes, generating significant theoretical power densities that have drawn considerable interest in NRED systems. However, due to poor scalability and severe ICP, the actual power density is substantially lower than theoretical predictions, posing challenges in meeting commercial demands. (See 3.2 Pore Density section for details)

Moreover, large pores, though exhibiting low resistance, are generally unsuitable for osmotic power generation from salinity gradients due to limited ion selectivity [68, 69]. Recent studies suggest that strong ion selectivity in large-scale charged pores, such as submicron or microscale charged pores, can be achieved by modifying the walls of conical pores with high surface charge densities [9, 68]. This modification induces nonlinear ion current rectification (ICR) behavior [10]. The synergy of ion selectivity and rectified ion transport properties positions these large-scale charged pores as a promising strategy to enhance osmotic power conversion [70]. For example, Gao *et al* [68] fabricated conical nanopores in 12 μm-thick poly(terephthalate) (PET) membranes using asymmetric ion track-etching technology and expanded the pore size to the microscale range through symmetric etching, achieving tip diameters between 216 nm and 810 nm. When the conical nanopores carried sufficiently high surface charges (-160 mC m^{-2}) in highly alkaline solutions (pH 11), this charge enhancement enabled the pores to rectify ion transport and exhibit ion selectivity, facilitating microscale osmotic power conversion (figure 3(d)). The study demonstrated that optimal power generation occurred at a tip diameter of 405 nm and a base diameter of 930 nm, with a maximum osmotic power output of 667 pW under a 1000-fold salinity gradient (figures 3(e) and (f)). Although highly charged pores could overcome the limitations of insignificant EDL overlap, ion selectivity

showed a significant decline when the pore size increased further (810 nm). Furthermore, similar pore-size-dependent power generation property has been demonstrated with the track-etched bullet-shaped nanochannels in PET membranes. Laucirica *et al* [70] found that these bullet-shaped nanochannels exhibit lower channel resistance, achieving a maximum osmotic power of 90 pW when the effective pore diameter is 380 nm. These studies expand the knowledge of osmotic power in solid-state pores from the nanoscale to the microscale, opening a promising avenue for achieving ultrahigh performance osmotic power generation.

3.2. Pore density

It is intuitively expected that osmotic power output increases proportionally with the number of nanopores in the membrane area (i.e. pore density) [59, 71]. A long-standing design principle for effective osmotic power generation has been to develop nanofluidic membranes with high pore density [72]. However, achieving high actual power density from the high theoretical power density estimated from single-pore models remains challenging for porous nanofluidic membranes [73]. Despite numerous attempts, the reported power density of NRED-based nanofluidic membranes is limited to only a few watts per square meter [73]. To understand and investigate the significant disparity in osmotic power density between single-pore and multi-pore membranes, several efforts have been conducted. A consistent conclusion is that the power density generated by multi-pore membranes is significantly lower than that of single-pore membranes, primarily due to the more pronounced ICP effect in the former. As pore density increases, severe ICP effects alter the solution concentration near the membrane surface [61]. On the high-concentration side, the membrane surface concentration ($C_{M,H}$) decreases compared to the bulk concentration ($C_{B,H}$), while the opposite occurs on the low-concentration side (figure 4(a)). This reduces the actual membrane potential and the driving force for diffusion transport, leading to lower ion selectivity. At the same time, the reduced salinity gradient near each pore entrance and the decreased transmembrane driving force result in fewer ions being transported through individual pores, leading to a reduction in the ionic conductance of each pore. As a result, increasing pore density does not linearly enhance the overall membrane conductance. Ultimately, these factors disrupt the osmotic power density, causing a significant deviation from simple linear extrapolation and showing an intensification of ICP with increasing boundary layer thickness. As research progresses, Xiao *et al* [74] discovered that in high pore density microscale charged pore arrays, each central pore is primarily influenced by up to four adjacent pores, with the influence of more distant pores being negligible (figure 4(b)). This finding provides theoretical support for pore–pore interactions at the microscale. Furthermore, it has been demonstrated that the output power density exhibits a local maximum dependence on pore density in nanofluidic membranes, contrary to traditional understanding. For example, Yazda *et al* [75] conducted a systematic experimental study on the effect of pore density on osmotic power density output using hybrid hexagonal boron nitride/silicon nitride (hBN/SiN_x) microscale nanopore arrays with adjustable pore spacings. Their experiments revealed a local maximum in power density caused by strong ICP effects at excessively close pore spacings ($<$500 nm). This result highlights the need for an optimal extrapolation from single-pore membranes to multi-pore arrays, requiring a fixed charged region around each pore (figure 4(c)).

To mitigate the ICP effect due to the microscale pore–pore interaction, researchers have attempted to introduce external fields, such as thermal gradients [78, 79] and cross-flows parallel to the membrane pores [80]. While these methods have somewhat alleviated the ICP effect, their effectiveness remains limited, and they face numerous constraints in practical applications. As research progressed, it has been discovered that constructing sub-nanopores while reducing pore spacing can alter microscale pore–pore interactions, enabling nanoscale pore–pore coupling effects governed by the Debye length and pore spacing [76]. For instance, Yang *et al* [76] achieved an unprecedented output power density exceeding 200 W m^{-2} using covalent organic framework (COF) monolayer membranes with well-ordered pore arrangements (figures 4(d) and (e)). This success is primarily attributed to the combination of sub-nanopore construction and reduced pore spacing, which suppresses current decay, enhances ion selectivity, and ultimately achieves practical power density levels, exhibiting distinct behavior compared to microscale charged pores (figure 4(f)). Similarly, Cheng *et al* [77] utilized 2D nanoporous polymer (2DNP) membranes with 2 nm pores to realize efficient osmotic power generation (figure 4(g)). Coarse-grained molecular dynamics simulations validated that there exists a narrow range of pore spacing in which both ion selectivity (S) and the net number of permeated charges (Q) remain high. Below this range, spatial constraints significantly hinder ion transport, leading to a low Q value; above this range, ion selectivity decreases, resulting in a low S value (figures 4(h) and (i)). By constructing sub-nanopores with reduced pore spacing, nanoscale pore–pore coupling effects governed by the Debye length and pore spacing can be achieved. This approach effectively suppresses the ICP effect under high pore density, enabling efficient osmotic power generation.

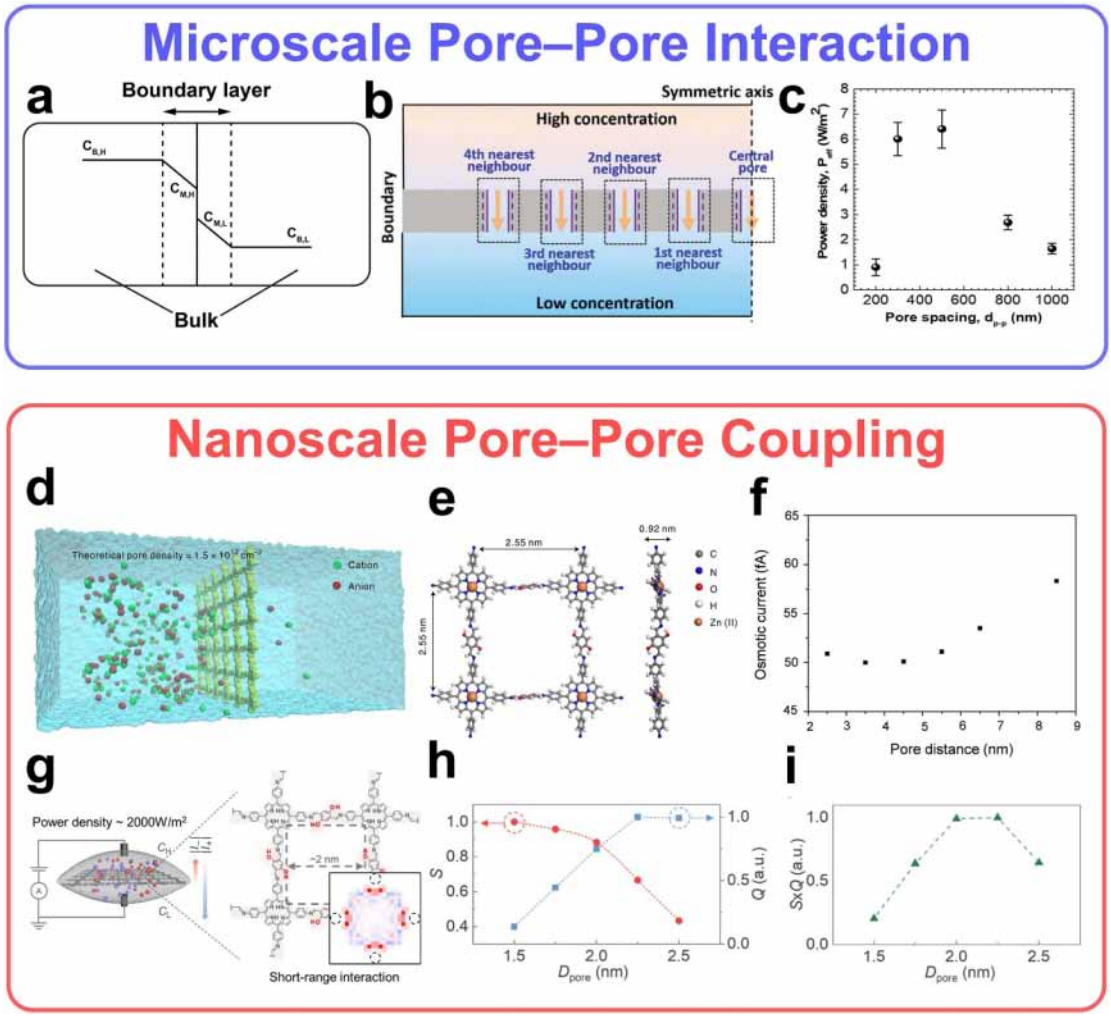

Figure 4. The effect of pore density on osmotic power conversion. (a) Schematic representation of ion concentration polarization (ICP). ICP reduces the transmembrane salinity gradient, and consequently the membrane potential decreases. (b) Schematic representation of the 4th nearest-neighbor with mirror symmetry. Reproduced from [74] with permission from the Royal Society of Chemistry. (c) Pore density effect on hBN/SiN_x nanopore arrays. Reprinted with permission from [75]. Copyright (2021) American Chemical Society. (d) Scheme of ion transport through the ZnTPP-COF monolayer membrane under a salinity gradient. (e) Simulated structure of ZnTPP-COF. (f) As the pore size decreases from 2.5 nm to 8.5 nm, the osmotic current of the central pore gradually increases. Reproduced from [76], with permission from Springer Nature. (g) Structural backbone of the 2D nanoporous polymer (2DNP) membrane. (h) S (ion selectivity, which is proportional to the generated osmotic potential) and Q (net number of permeated charges, representing osmotic current) as a function of D_{pore}. (i) Power output of the membrane ($S \times Q$) as a function of D_{pore}. Reprinted with permission from [77]. Copyright (2023) American Chemical Society.

3.3. Charge density

The charge density of nanopores, including surface charge density and space charge density, is another key factor influencing ion transport dynamics [81, 82]. For surface charge density, it was traditionally believed that higher surface charge densities within the pores lead to enhanced ion selectivity and increased output power density [83, 84]. For example, based on this design principle, Siria *et al* [32] fabricated a single transmembrane BNNT with an anticipated ultrahigh density of chargeable sites (up to 18 sites nm^{-2}). Due to interfacial chemical reactions ($BN_3 + H_2O \rightarrow BN_3 - OH + H^+$), the surface charge of BNNTs can be tuned by adjusting the solution pH. As the pH increased from 5.5 to 11, the surface charge rose from approximately 0.1 C m^{-2} to 1 C m^{-2}, resulting in a maximum power density of up to 4 kW m^{-2} under a pH of 11 and a 1000-fold KCl salinity gradient. However, recent studies have revealed that the effective location of the surface charge varies depending on the pore length. Cao *et al* [69] constructed three different charged models based on precise Poisson and Nernst–Planck models: (i) both the membrane surface and nanopore wall are charged (figure 5(a)), (ii) only the membrane surface is charged (figure 5(b)), and (iii) only the nanopore wall is charged (figure 5(c)). Theoretical calculations demonstrated that for shorter nanopores ($L = 2$ nm), ion selectivity and net diffusion current are primarily influenced by the membrane surface charge. In contrast, for longer nanopores ($L = 1000$ nm), the surface charge on the nanopore walls plays a dominant role. This finding highlights that nanopore length is a critical factor in determining the effect of

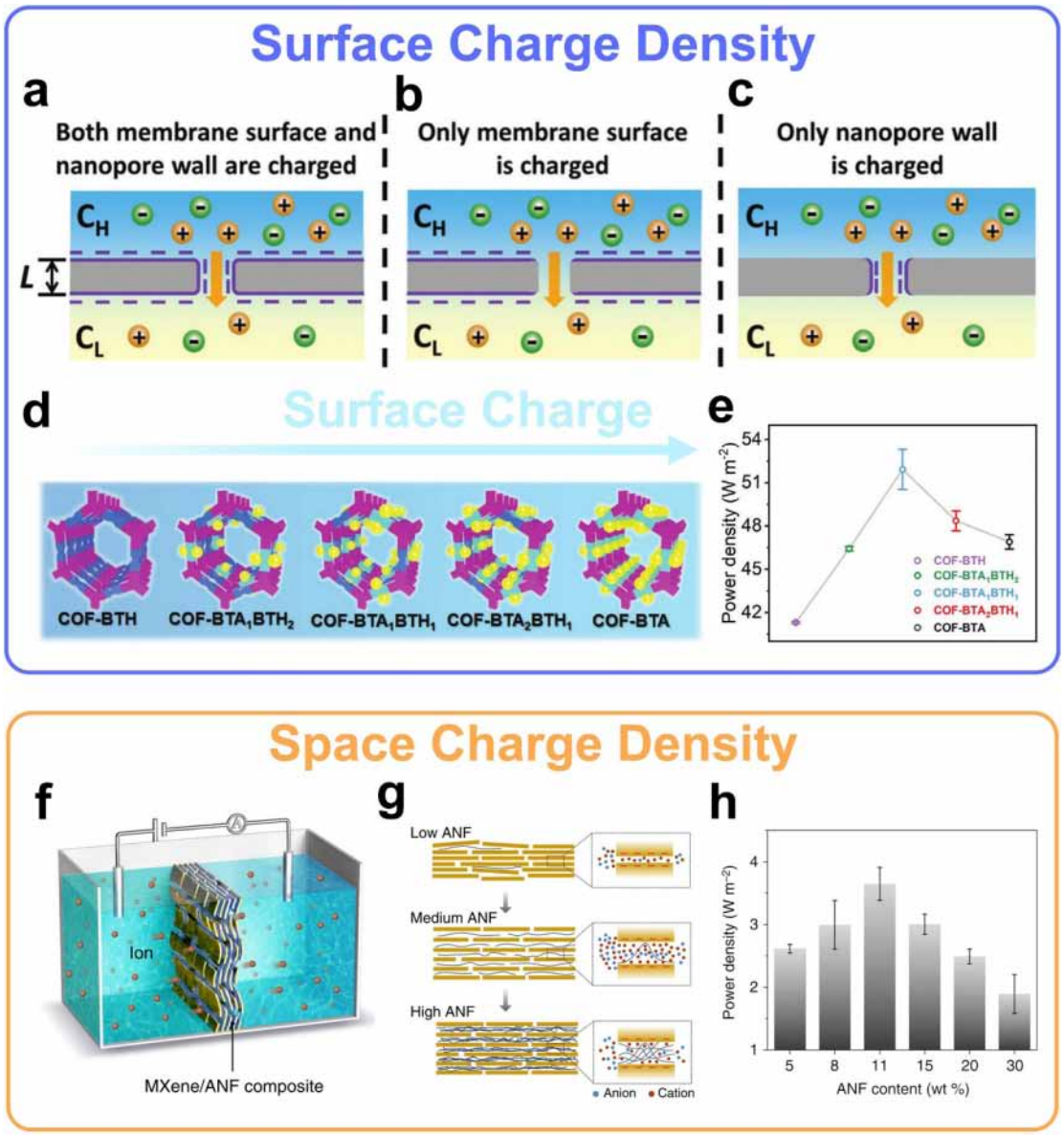

Figure 5. The effect of surface charge and space charge on osmotic power conversion. (a) Schematic of both the membrane surface and nanopore wall were charged model. (b) Schematic of only the outer membrane surface was charged model. (c) Schematic of only the nanopore wall was charged model. [69] John Wiley & Sons. (© 2018 WILEY-VCH Verlag GmbH & Co. KGaA, Weinheim). (d) COF-based nanofluidic membranes with varied charge densities. (e) Experimental demonstration of the local maximum dependence of osmotic power on surface charge density using COF-based nanofluidic membranes. [86] John Wiley & Sons. (© 2021 Wiley-VCH GmbH). (f) Schematic of MXene/ANF osmotic power source. (g) Schematic of the influence of the ANF content on the energy conversion process. (h) Experimental demonstration of the local maximum dependence of osmotic power on space charge density using MXene/ANF nanofluidic membranes. Reproduced from [87]. CC BY 4.0.

surface charge on ion transport dynamics. Furthermore, a higher surface charge density does not necessarily result in higher output power density. Hsu *et al* [85] demonstrated through theoretical simulations and experiments that excessively high surface charge in a single nanoconfined channel significantly enhances the ICP effect, thereby weakening the effective salinity gradient and reducing overall performance. Subsequently, Cao *et al* [69] fabricated COF-based nanofluidic membranes with surface charge densities ranging from 0.007 to 0.18 C m^{-2} by adjusting the ratio of ionic and non-ionic components during synthesis (figure 5(d)). Notably, COF membranes with moderate charge density (0.085 C m^{-2}) exhibited the highest osmotic power density (figure 5(e)). Due to the presence of pore−pore interactions in porous membrane systems, ICP effect will be more pronounced compared to single nanopores, leading to a more profound and complex influence of surface charge on nanofluidic osmotic power conversion.

In addition to surface charge, researchers have introduced charged nanofibers (e.g. cellulose nanofiber (CNF) [88], aramid nanofiber (ANF) [87, 89], and bacterial nanocellulose (BNC) [90], etc [91, 92]) into inherently charged nanoconfined channels. These 1D nanofibers form interlocking structures by bonding

with channel-forming nanosheets through hydrogen or chemical bonds. Rich in functional groups (e.g. hydroxyl, carboxyl), the nanofibers introduce space charges into nanoconfined channels, effectively enhancing ion selectivity [83, 87]. Simultaneously, the inclusion of nanofibers and the formation of interlocking structures improve channel stability and dimensions, which macroscopically enhance both ion flux and the mechanical strength of the nanofluidic membrane [89, 92]. For example, Zhu *et al* [89] assembled composite membranes of metallic-phase MoS_2 (M–MoS_2) and CNF using vacuum filtration, significantly improving mechanical strength and ion selectivity. Under natural seawater and river water conditions, they could achieve a high power density of 6.7 W m^{-2}. Similarly, Zhang *et al* [87] investigated the ion transport enhancement mechanisms of composite membranes self-assembled from MXene and ANF (figure 5(f)). Experimental results showed that ANF enlarges ion channel dimensions, increases ion flux, and introduces sufficient space charges, enabling EDL overlap and high ion selectivity. This ultimately led to the construction of low-resistance nanoconfined channels. However, when the ANF content was too high, it physically blocked the channels, resulting in channel discontinuity, reduced effective pore size, and increased transport resistance (figure 5(g)). Therefore, osmotic power generation exhibits a local maximum dependence on the space charge effect (i.e. ANF content) (figure 5(h)). And the continuum-based theoretical simulations revealed a synergistic relationship between surface charge and space charge. This synergy becomes most significant when the contributions of surface charge and space charge to ion transport are comparable. If one dominates while the other is weak, the synergistic effect is diminished. This work provides an important paradigm for future investigations into the relationship between surface charge and space charge in nanofluidic membranes.

3.4. Membrane thickness

In the past, it was widely believed that reducing the thickness of nanofluidic membranes (i.e. the length L of the pores or channels) could decrease resistance, increase ion flux, and significantly enhance output power density by improving permeability [93]. The thinner the better, became one of the important design principles of membrane. However, recent theoretical studies have shown a counterintuitive channel-length dependence in the process of osmotic power conversion [94, 95]. Cao *et al* [95] found that for very short nanochannels ($L < 400$ nm), the osmotic power decreases continuously as the channel length L reduces, exhibiting an abnormal non-Ohmic response (figure 6(a)). Thermodynamic analysis and numerical simulations demonstrated that a very short channel length ($L = 50$ nm) weakened the charge selectivity of the nanochannel and induced strong ICP (figure 6(b)). In contrast, for long nanochannels ($L = 5000$ nm), no significant ICP was observed, and the effective transmembrane salinity gradient was generally consistent with the applied bulk values (figure 6(c)). In short nanochannels ($L = 50$ nm), strong ICP was observed, with accumulated ions penetrating deeply into the nanochannel at the low-concentration end. The effective salinity gradient in short nanochannels showed a nonlinear increase with the applied salinity gradient, significantly deviating from the bulk value, especially under the high salinity gradients (figure 6(c)). This work reveals an element that has long been overlooked: channel length L, and its importance in nanofluidic energy conversion, providing important guidance for the subsequent design of high-performance NRED systems. Additionally, Su *et al* [93] explored alumina nanochannels with different charge properties and observed a similar phenomenon of local maximum dependence of osmotic power density on channel length (figure 6(d)). Whether in cation-selective or anion-selective channels, when the channel length is sufficiently short, the ICP effect dominates the channel length-dependent osmotic power behavior, leading to a significant decrease in effective salinity gradient and ion selectivity. Ultimately, the power output decreases significantly with a reduction in channel length (figure 6(e)). Similarly, Chen *et al* [94] used silk fibroin to prepare an ultra-thin membrane with excellent mechanical properties, where the membrane thickness could range from 20 nm to 700 nm without significantly affecting its mechanical properties (Young's modulus and hardness). However, when the membrane thickness was less than 100 nm, the current density reached a plateau at 225 A m^{-2}, while for membranes thicker than 100 nm, membrane resistance showed an Ohmic response with increasing membrane thickness, ultimately achieving a peak power density of 4.06 W m^{-2} at a thickness of 100 nm due to the combination of ICP effect and membrane resistance (figures 6(f)–(h)). These works systematically investigated the power performance dependence on membrane thickness (channel length L) from both theoretical and experimental perspectives, providing direction for the design and optimization of high-performance nanofluidic membranes.

3.5. Ion transport pathway

With the advancement of emerging micro-nano fabrication technologies and advanced materials, it has become possible to explore energy harvesting using various novel nanofluidic membranes under salinity gradients. To achieve high power density, it is necessary to improve both membrane selectivity and permeability. However, ion transport pathway, which play a crucial role in membrane permeability, have

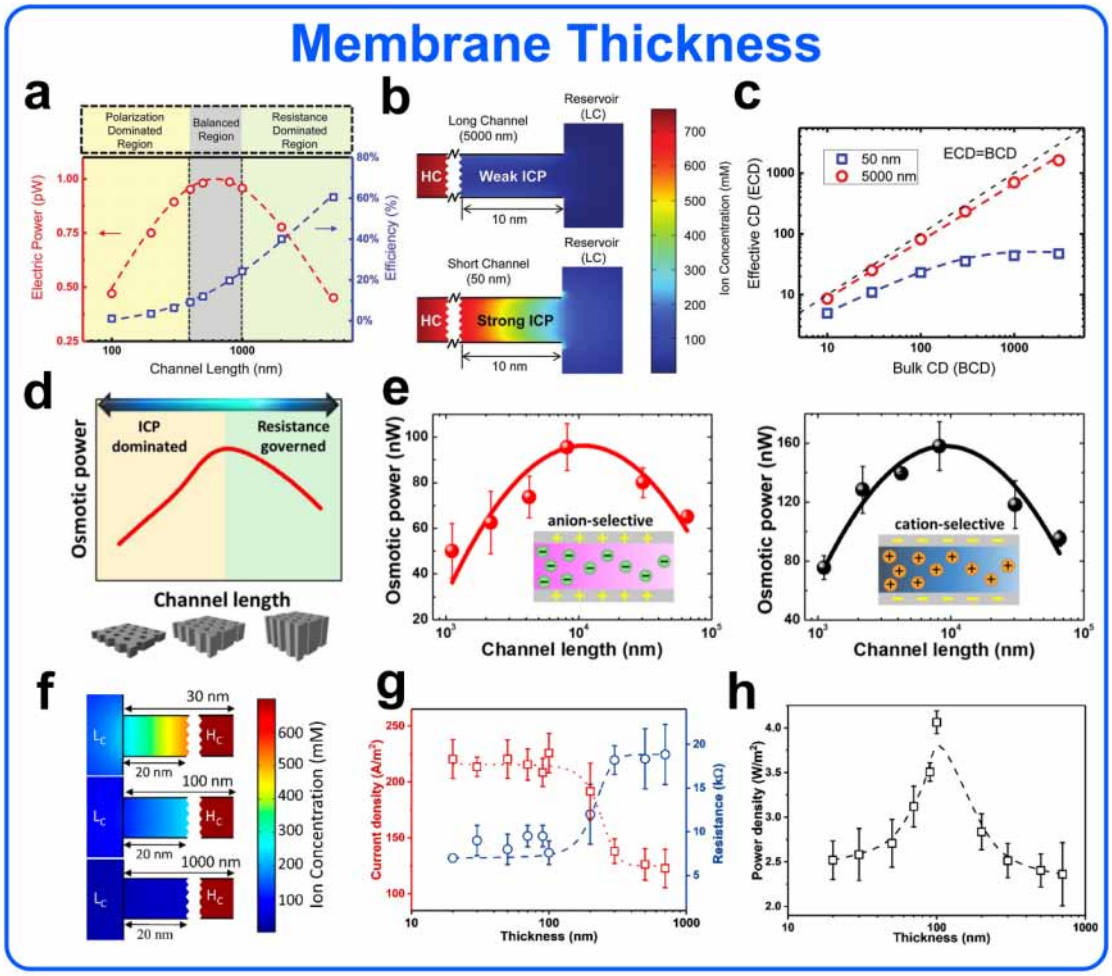

Figure 6. The effect of membrane thickness on osmotic power conversion. (a) Theoretical demonstration of the pore-length-dependent osmotic power behavior. (b) For excessively short nanopores, the significant ICP effect enables the decreasing power output with the decrease of pore length. (c) The relationship between the effective salinity gradient (ECD) and the applied bulk salinity gradient (BCD). The dashed black line indicates the relationship of ECD = BCD. In long nanochannels (circle), the ECD generally agrees with the BCD. In short nanochannels (square), the ECD shows a nonlinear growth with the BCD, and it remarkably deviates from the bulk value. [95] John Wiley & Sons. (© 2017 WILEY-VCH Verlag GmbH & Co. KGaA, Weinheim). (d) The power output could be maximized at an optimal design of membrane channel length. (e) Experimental results demonstrating the local maximum dependence of pore length on osmotic power using length-controllable ANMs, independent of the surface charged natures. Reprinted from [93], Copyright (2021), with permission from Elsevier. (f) Three models with different channel lengths from 30 nm to 1000 nm. (g) With the decreasing thickness, the current density increases until it reaches a plateau of 225 A m^{-2}. The corresponding resistance shows an inverse tendency with the current density. When the thickness of the membrane is less than 100 nm, the constant reservoir resistance and the reservoir/nanopore interfacial resistance become the primary factors. When the thickness is >100 nm, the resistance of the membrane is predominant, showing Ohm-like dependence that increases with thickness. (h) In a balance of polarization and Ohmic effects, the power density peaks at 4.06 W m^{-2} when the thickness is 100 nm. Reprinted with permission from [94]. Copyright (2020) American Chemical Society.

been largely overlooked in the past [96–98]. Here, we focus on three strategies to optimize ion transport pathway: horizontal transport [98, 99], 1D/2D synergistic transport [100, 101], and ordered pore structure [102–104]. These strategies aim to achieve high ion transport flux while maintaining high ion selectivity, enabling efficient osmotic power conversion.

In the past, researchers used self-assembly strategies to stack 2D nanosheets, forming nanoconfined channels with uniform interlayer spacing, enabling efficient ion transport with high selectivity. However, ion transport occurred along the normal direction of the membrane (i.e. vertical transport). Despite high ion selectivity, the unusually long ion transport pathway led to lower ion flux and current density, resulting in suboptimal power density. For example, Zhang *et al* [87], even after enhancing transport performance by introducing space charge, achieved only a power density of 4.1 W m^{-2}, which does not meet commercialization requirements (5 W m^{-2}). In response, inspired by the fast water transport in xylem vessel elements, Qian *et al* [99] altered the ion transport direction from vertical to horizontal transport with straight and short pathway, significantly reducing the ion transport resistance (figure 7(a)). The horizontal ion transport MXene (H-MXene) can withstand extreme saline–alkali conditions and exhibits superior ion selectivity and permeability compared to vertical ion transport channels (V-MXene). It achieved a current

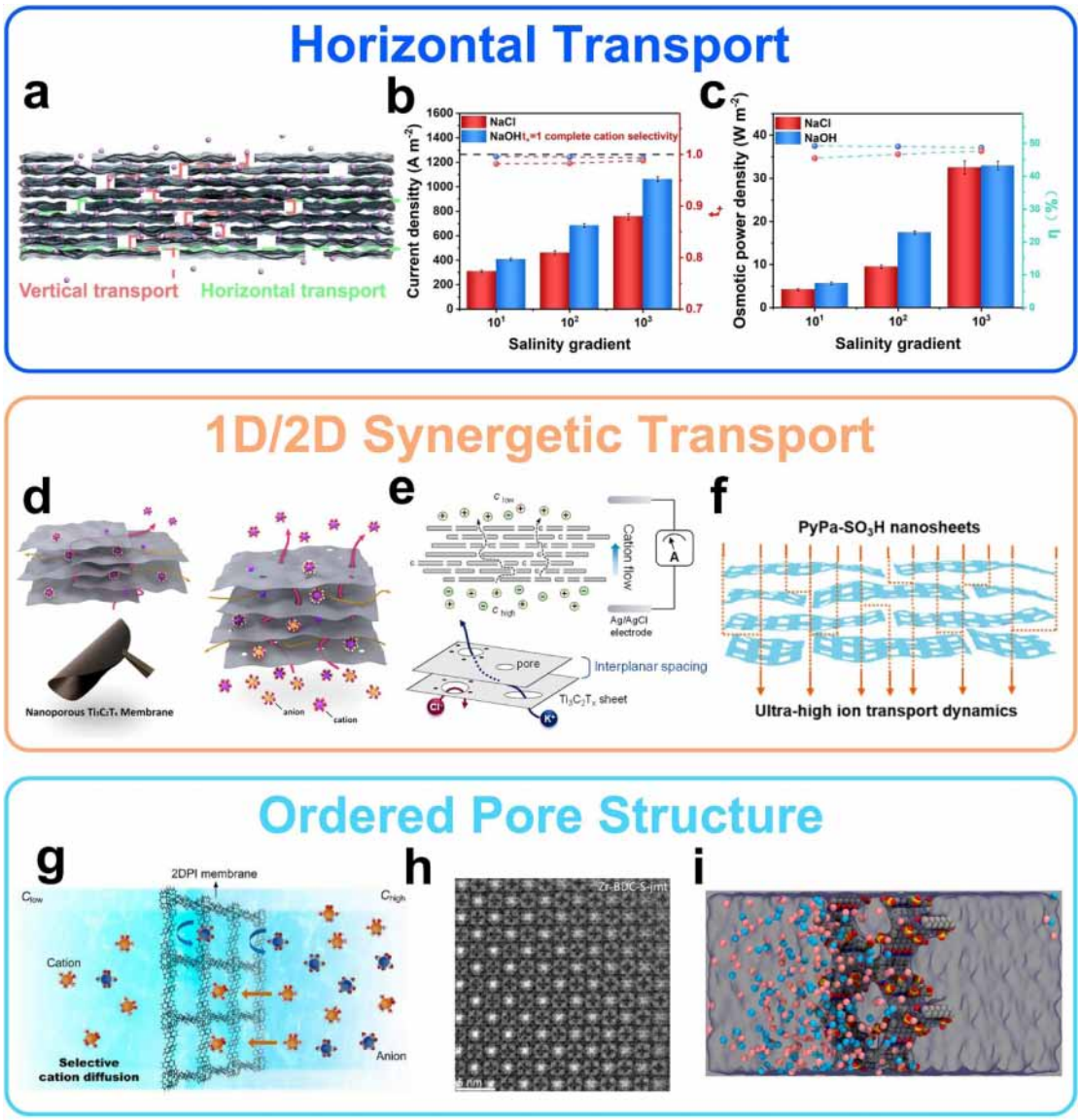

Figure 7. The effect of ion transport pathway on osmotic power conversion. (a) Schematic of different transport pathways in in nanoconfined channels. (b) The diffusion current density and cation transference numbers (t_+) of H-MXene osmotic power source at different salinity gradients of NaCl and NaOH solutions. (c) The osmotic power density and energy conversion efficiency (η) of H-MXene osmotic power source at different salinity gradients of NaCl and NaOH solutions. [99] John Wiley & Sons. (© 2024 Wiley-VCH GmbH). (d) Schematic of ion transport through the chemically etched nanopore and 2D slit channels in lamellar MXene membranes. (e) The cation-selective membrane facilitates the transport of cations through its etched nanopores and 2D slits, while electrostatically repelling anions, thereby establishing an electrical gradient across the membrane. Reproduced from [101]. CC BY 4.0. (f) The ion migration pathway through stacked PyPa-SO3H nanosheets in the both horizontal and vertical directions. Reprinted with permission from [100]. Copyright (2021) American Chemical Society. (g) Schematic of the selective ion diffusion process across the imine-based 2D polymer (2DPI) membrane. Reproduced from [104]. CC BY 4.0. (h) High resolution transmission electron microscopy (HRTEM) image showing ordered pore structure of Zr-MOF membrane. Reprinted with permission from [103]. Copyright (2024) American Chemical Society. (i) Typical simulation box showing oriented COF−xSO$_3$H membrane and electrolytes. Reprinted with permission from [102]. Copyright (2022) American Chemical Society.

density more than three orders of magnitude higher without significant polarization, with an osmotic power density of 9.47 W m^{-2} and an energy conversion efficiency of 45.7% (figures 7(b) and (c)). Molecular dynamics simulations show that MXene nanochannels exhibit excellent cation selectivity, with the diffusion coefficients of Na^+ and H^+ significantly higher in H-MXene than in V-MXene. Specifically, the transport rates of Na^+ and H^+ in H-MXene are 2.57 times and 2.32 times those in V-MXene, respectively. This work demonstrates that H-MXene with horizontal ion transport channels achieves a balance between selectivity and permeability, bridging the gap in salinity-gradient-driven energy conversion in saline–alkali environments.

In addition to shortening the ion transport path by altering the direction of ion transport, optimizing the ion transport path can also be achieved by selecting appropriate materials and modification engineering. For example, Hong *et al* [101] oxidized the original MXene nanosheets with sulfuric acid, creating nanopores

with diameter of approximate 10 nm in the nanosheet, which was then self-assembled into a membrane through vacuum filtration (figure 7(d)). The existence of 1D nanopores between layers provides additional channels for cation transport, optimizing the ion transport pathway (figure 7(e)). Benefiting from this 1D nanopore and 2D nanopore synergetic ion transport mechanism, the porous MXene membrane achieved a maximum power density of 17.5 W m^{-2}, a 38% improvement compared to the original MXene membrane. In a similar vein, Man *et al* [100] proposed a comparable concept by fabricating composite membranes made from 2D sulfonated COF (PyPa–SO_3H) nanosheets and styrene sulfonate sodium grafted ANFs (SANF). The SANF provides sufficient space charge and improves the mechanical properties of the membrane, ensuring high ion selectivity, while the abundant 1D nanopores on the COF nanosheets offer additional pathways for ion transport, forming a similar 1D/2D synergetic transport effect (figure 7(f)). The unique ion transference phenomena of PyPa-SO_3H nanosheets were calculated by density functional theory. They compared the migration energy barriers for vertical transport, horizontal transport, and 1D/2D synergetic transport. The energy barriers were found to be 0.8 eV, 0.78 eV, and 0.69 eV, respectively, demonstrating that 1D/2D synergetic transport mechanism significantly reduces ion transport resistance, greatly increasing the transmembrane ion flux and power density in osmotic power generation.

Another effective strategy to optimize ion transport pathways is to construct ordered pore structures with ultrathin thickness using highly ion-selective materials, such as polymer materials, COF, and metal organic framework (MOF). For example, Zhang *et al* [104] demonstrated a 2D imine-based polymer (2DPI) ultrathin membrane, which combines excellent ion conductivity with high selectivity for energy conversion (figure 7(g)). This highly ordered ultrathin membrane, with large numbers of hydroxyl groups ($\sim 1.5 \times 10^{27}$ m^{-3}), exhibits excellent selective permeability for cations, achieving a maximum power density of 53 W m^{-2}. Additionally, Chen *et al* [103] used phase engineering to transform a synthesized Zr-based MOF from its initial **fcu** topology to a defective **jmt** phase (figure 7(h)). These defects act as ordered 1D nanochannels, exhibiting ultra-high ion selectivity ($t_+ = 0.977$) while significantly increasing ion flux, achieving a peak power density of 10 W m^{-2} under artificial seawater and river water conditions. Similarly, Cao *et al* [102] overcame the long-standing challenges of ordered pore structure COF by precisely controlling both the structural orientation and charge polarity of the nanochannels, successfully preparing highly ordered vertically aligned 1D nanochannels (figure 7(i)). This approach enabled tunable ion transport properties and effective energy conversion, achieving a power density of 228.9 W m^{-2}, highlighting the enormous potential of directionally ordered ultrathin COF materials in ion-selective transport.

3.6. Structure design

Inspired by biological ion channels, IEMs with ICR effect have been developed [105, 106]. These membranes achieve selective, directional, and amplified ion transport by designing asymmetric properties along the ion transport direction, such as pore sizes, pore geometries, and surface charges. This asymmetric structural configuration was therefore conventionally designated as ionic diode membrane (IDM) in the literature, reflecting its functional analogy to electronic diodes in governing asymmetrical ion transport behavior. This strategy significantly enhances both current and power output [107, 108]. The structure design of the asymmetric properties is primarily achieved through Janus structures composed of two materials with distinct properties [109, 110]. By leveraging differences in surface charge and pore size, the membranes exhibit improved ion selectivity and permeability, providing an optimized pathway for efficient osmotic power generation [111, 112]. This section is classified based on pore sizes, starting with the introduction of sub-nanoscale Janus structures with pore sizes smaller than 2 nm. For instance, Ding *et al* [111] developed a bioinspired sub-nanoscale Janus membrane based on modified MXene materials. This membrane comprises a positively charged MXene (PCM) layer and a negatively charged MXene (NCM) layer, which are anion-selectivity and cation-selectivity, respectively (figure 8(a)). The structure resembles an ionic p–n junction, analogous to the p–n junction in semiconductor systems, enabling a rectification ratio of 15.4 at a concentration of 10^{-3} M. This rectification performance primarily arises from distinct ionic states (enrichment or depletion) under different voltage biases. The Janus structure, characterized by charge polarity, not only enhances directional ion transport but also mitigates ICP effect, improving osmotic power generation efficiency and achieving a power density of 8.6 W m^{-2}. Cao *et al* [108] proposed a COF-based Janus IDM constructed from a negatively charged TpPa-SO_3Na layer and a positively charged TpEB layer, with charge polarity derived from sulfonate and quaternary ammonium functional groups. This Janus sub-nanoscale structure achieves directional anion-selective transport by forming ion enrichment zones (figure 8(b)) and ion depletion zones (figure 8(c)), optimizing transport efficiency through a combination of ionic diffusion coefficients and electrostatic interactions. This membrane delivers a power density of up to 210.1 W m^{-2} under a 50-fold NaI gradient, significantly outperforming existing Janus designs, highlighting its potential for energy conversion and ion sieving applications.

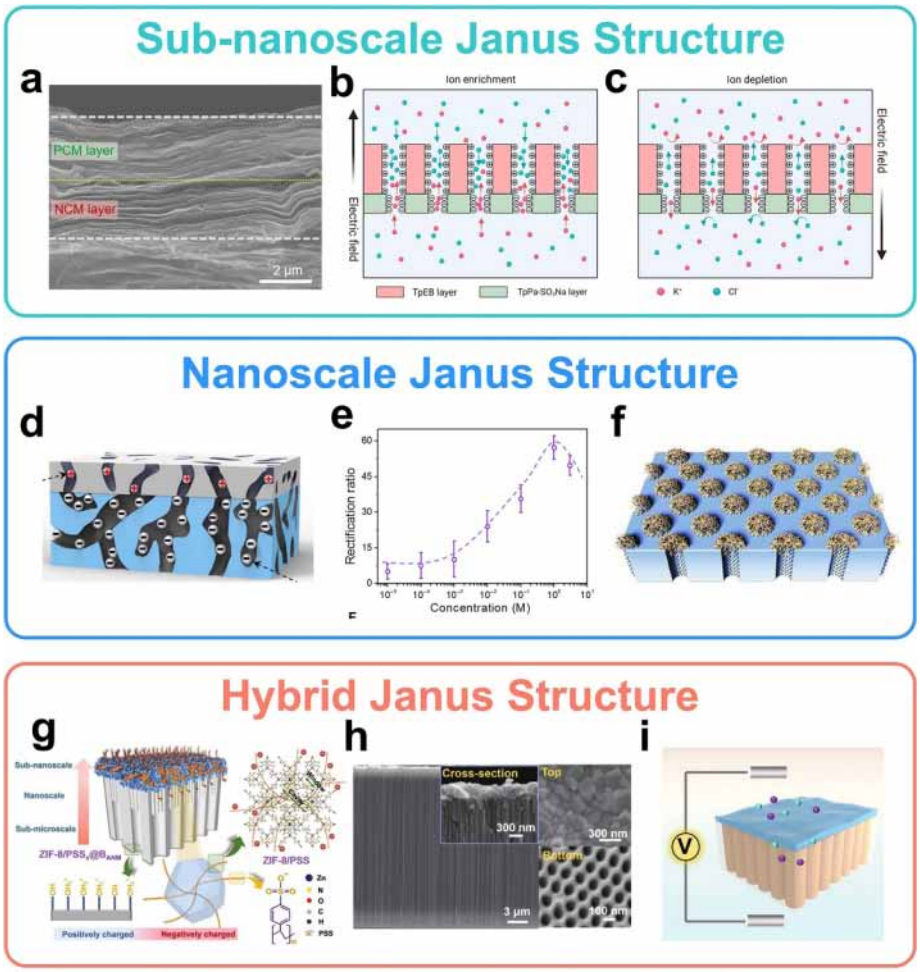

Figure 8. The effect of structure design on osmotic power conversion. (a) The SEM images of Janus structure of MXene membrane. [111] John Wiley & Sons. (© 2022 Wiley-VCH GmbH). Illustration of ionic diode effect, originating from the (b) ion enrichment and (c) ion depletion in the heterojunctions. Reprinted with permission from [108]. Copyright (2022) American Chemical Society. (d) Schematic of the cross section of the Janus structure with 3D pores. (e) Rectification ratio of the Janus membrane under a series of KCl solution concentration. From [113]. Reprinted with permission from AAAS. (f) The formation of robust h-PEI-capped Janus nanochannels by amidation reaction. From [110]. Reprinted with permission from AAAS. (g) Schematic of the ZIF-8/PSSx@BANM with a tri-continuous pore structure from sub-microscale to sub-nanoscale and asymmetric charges. The thin ZIF-8/PSS layer is characterized with angstrom-scale window-cavity structures and the Janus membrane is composed of large sub-microscale stem channels and small nanoscale branched channels. (h) The SEM images showing that a ZIF-8/PSS layer can be continuously grown on the branched channel sides of Janus membrane. [112] John Wiley & Sons. (© 2023 Wiley-VCH GmbH). (i) The structure HOF/AAO Janus membrane. [114] John Wiley & Sons. (© 2024 Wiley-VCH GmbH).

Nanoscale Janus structures have also been extensively studied. For instance, Zhu *et al* [113] reported a NRED system based on a Janus 3D porous membrane composed of negatively charged PAEK-HS and positively charged PES-Py ionic polymers. The charge polarity originates from sulfonate groups (negative charge) and pyridine groups (positive charge). The pore sizes of PAEK-HS and PES-Py are approximately 17.1 nm and 8.5 nm, respectively, enabling efficient ion transport through precise control of surface charge density and porosity. Remarkably, the Janus membrane exhibited the highest rectification ratio (∼57.2) in 1 M KCl solution and maintained a high rectification ratio (∼49.7) even in 3 M KCl solution (figure 8(e)). Leveraging this ion rectification effect, the membrane achieved unidirectional anion transport under high salinity gradients, with a power density of 5.10 W m^{-2} at a 500-fold salinity gradient. This nanoscale Janus membrane design demonstrates stable performance in high-salinity environments, significantly enhancing osmotic power generation efficiency and offering a novel approach for the scalable fabrication and practical application of high-performance membrane materials. Moreover, Li *et al* [110] proposed a Janus membrane based on a mushroom-shaped nanochannel array for efficient osmotic power generation. The membrane consists of negatively charged 1D stem-like nanochannels and positively charged cap-like 3D channel networks (figure 8(f)). The charge polarity is achieved through carboxylate groups embedded in polymers for the stem and chemically modified hyperbranched polyethyleneimine (h-PEI) for the cap. The directional ion rectification mechanism enabled by the Janus structure provides exceptional anion selectivity, effectively suppressing reverse ion leakage. Under a 500-fold salinity gradient, the membrane achieved a power density

of 22.4 W m^{-2}, which further increased to 33.2 W m^{-2} under a 1000-fold gradient. This work introduces an ultra-high-density (10^{12} cm^{-2}) mushroom-shaped Janus nanochannel design, achieving unprecedented efficiency in osmotic power generation and offering a novel pathway for large-scale industrial clean energy harvesting.

Recently, to further enhance osmotic power conversion efficiency, hybrid Janus structures featuring different scale of channels have been introduced into membrane design. In 2024, Fauziah and Yeh [112] proposed a hybrid Janus structure with sub-nanometer pores, combining MOF (ZIF-8) and aligned branch-type alumina nanochannel membrane (BANM) to create a three-tier pore structure, ranging from sub-nanoscale (∼4.8 Å windows in ZIF-8) to nanoscale (branch channels of ∼23 nm in BANM) and sub-microscale (main channels of ∼100 nm in BANM) (figures 8(g) and (h)). The negatively charged ZIF-8/PSS layer is formed through sulfonate functionalization, while the positively charged BANM layer is obtained via anodic oxidation surface modification of alumina. With an enhanced pore size gradient and ion diode effect, the membrane facilitates rapid unidirectional cation (e.g. Li^+) transport while effectively suppressing reverse ion leakage. In organic solvents (e.g. LiCl-methanol), the membrane achieves a power density of 9.58 W m^{-2} under a 50-fold LiCl gradient and reaches a maximum of 50.5 W m^{-2} by mixing a 2 m LiCl-methanol and pure methanol solutions, significantly outperforming conventional membranes. This work provides a solution for efficient osmotic power generation and ion-selective separation in organic solvents, offering important insights for the development of next-generation NRED systems. Additionally, Wang *et al* [114] proposed hybrid structure Janus membrane based on hydrogen-bonded organic frameworks (HOF) and anodic aluminum oxide (AAO) for efficient osmotic power generation (figure 8(i)). The HOF layer is *in situ* grown on the AAO surface using H_4TBAPy (1,3,6,8-Tetramolecular (p benzoic acid) pyrene) molecules, exhibiting significant negative charge characteristics (surface charge density of −0.182 C m^{-2}), while the AAO substrate, prepared via anodization, provides stable positive charge properties. The pore size of HOF is approximately 2.5 nm, and the channel diameter of AAO is around 50 nm. The combination of hydrogen bonding and π–π stacking interactions enhances the structural stability. With asymmetric surface charge distribution and an efficient ion rectification mechanism, the membrane successfully inhibits ICP effect that occurs at the low concentration side and effectively suppresses reverse current to reduce power loss. Under a 500-fold salinity gradient, the membrane achieved a power density of 75.2 W m^{-2}, which further increased to 94.2 W m^{-2} under alkaline conditions (pH 11). This work develops a stable and efficient HOF-based Janus membrane through hydrogen-bond-driven self-assembly, significantly enhancing osmotic power generation efficiency. It also demonstrates potential in practical applications such as antifouling and self-cleaning, offering new insights for next-generation NRED technology.

3.7. External fields

Applying external fields is also a significant approach to enhancing ion transport dynamics in NRED systems [115, 116]. When osmotic power is coupled with different external fields, it can increase the ionic driving force, thereby enhancing ion flux and ultimately achieving a trade-off between ion selectivity and permeability. Common external fields coupled with osmotic effects include chemical fields [50, 115–118], thermal fields [78, 79, 90, 119, 120], light fields [121–125], pH fields [126–128], ionic fields [129], and mechanical fields [130, 131]. For instance, when osmotic power is coupled with a chemical field, chem-osmotic coupling can be established. In 2015, Wei [29] proposed a osmotic power source based on GO and partially reduced GO (rGO), which regulates ion transport under chem-osmotic coupling by leveraging the super-permeability of water molecules and ion conductivity in GO. A high surface charge density and nanoconfined effect were achieved by coating PEDOT, GO ink, and rGO ink on an Ag charge collectors, creating nanoconfined channels on any insulating substrate (e.g. polymer sheets/paper). The energy of this GO-based osmotic power source depends on its length, and when room-temperature ionic liquid (RTIL) was added, a monomeric cell with a length of 0.5 cm can generate an energy capacity of 30 Ah L^{-1} at a voltage of up to 0.7 V (figure 9(a)). This work, for the first time, utilizes the fast water transport properties of GO to construct a printable, flexible chem-osmotic coupling osmotic power source, providing a low-cost, environmentally friendly energy solution for wearable devices and humidity sensors. In 2021, Yang *et al* [117] proposed a bioinspired, humidity-driven all-solid-state osmotic power source, achieving efficient conversion of ion gradients to electrical energy through chem-osmotic coupling. The device utilizes GO and rGO as materials, constructing an osmotic power source with GO-based inks of two different ion concentrations. The device leverages a humidity-activated K^+ gradient and unique ion dynamics in nanoconfined channels to achieve ion transport and chem-osmotic coupling (figure 9(b)). By optimizing the printing design, the device achieved an ultra-high open-circuit voltage of 192 V and a power density of 2.5 mW cm^{-3}, rivaling thin-film lithium batteries. This work introduces the electrochemical field generated by redox reactions into osmotic effect through chem-osmotic coupling, increasing ion migration driving forces and ion currents, providing a novel solution for low-cost, environmentally friendly, and portable

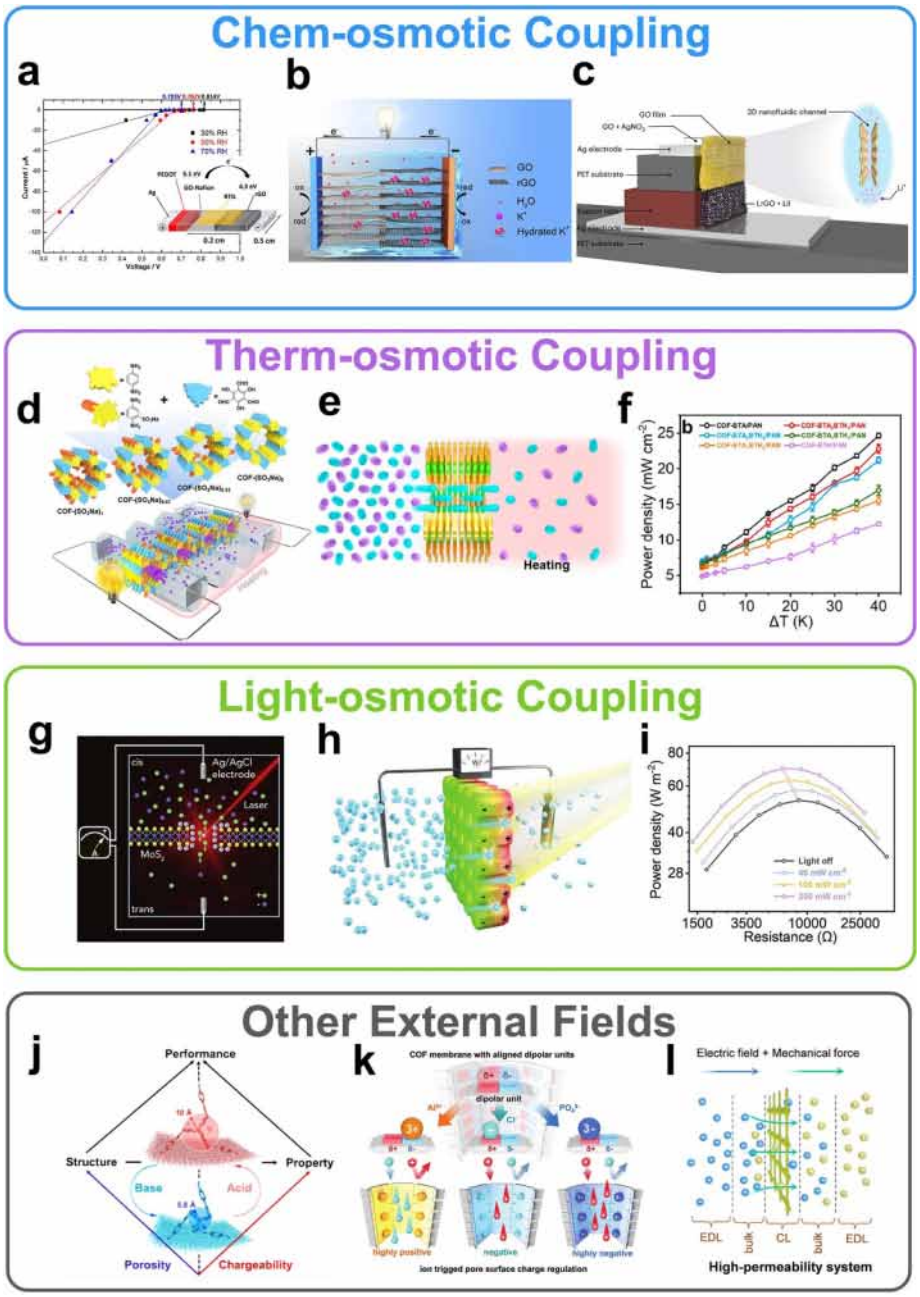

Figure 9. The effect of external fields on osmotic power conversion. (a) *I–V* characteristics of PEDOT/GO-Nafion/rGO battery that was coated on polymer substrate of polyethylene naphthalate (PEN) with RTIL under different relative humidity (RH) of 30%, 50% and 70%. Reproduced from [29]. CC BY 4.0. (b) The osmotic power source is composed of GO inks and rGO inks with different ion concentrations and a pair of silver electrodes. In the presence of moisture, the chemical potential energy of the ion gradient is converted to electric energy via directional ion migration and redox reactions and thus produces electric power. Reproduced with permission from [117]. (© 2021. Published under the PNAS license). (c) Schematic illustration of the vertical structure and mechanism of Li^+ transport within the 2D nanoconfined channels. Reproduced from [118], with permission from Springer Nature. (d) Conceptual illustration of the conversion of energies derived from low-grade heat and salinity gradient into electricity using ionic COF membranes. [120] John Wiley & Sons. (© 2022 Wiley-VCH GmbH). (e) Ion transport through a permselective membrane with alleviated ICP by increasing the hydrodynamic convection effects via introducing a temperature gradient. (f) Plots of the output power density of COF membranes versus temperature gradient. Reprinted with permission from [79]. Copyright (2022) American Chemical Society. (g) Schematics of the experimental setup: laser light is used to photogate the MoS_2 and thus modulate the surface charge of the nanopore. Reprinted from [125], Copyright (2019), with permission from Elsevier. (h) These photoelectric-responsive membranes generate a built-in electric field when exposed to light, mitigating ICP effect and facilitating directed ion transport. (i) Osmotic power density with illumination under 40, 100, or 200 mW cm^{-2} xenon lamp. [121] John Wiley & Sons. (© 2024 Wiley-VCH GmbH). (j) A smart polycage membrane with responsive osmotic power generation based on synchronously switchable sicroporosity and chargeability. Reprinted with permission from [126]. Copyright (2024) American Chemical Society. (k) Illustrates the dynamic ion–dipole interactions within the channels of the COF membrane, which precisely regulate the charges on the pore surfaces and permselectivity in terms of both nature and intensity through association with various ions. [129] John Wiley & Sons. (© 2024 Wiley-VCH GmbH). (l) Schematic illustration of ion transport by the and coupled electric field and mechanical pressure in a highly permeable COF monolayer. Reprinted with permission from [130]. Copyright (2023) American Chemical Society.

osmotic power devices. Moreover, Yang *et al* [118] proposed a vertical osmotic power source based on GO, partially rGO, and interfacial redox reactions (figure 9(c)). Chem-osmotic coupling was achieved by constructing ion gradients and redox reaction interfaces at the GO/rGO junction, where GO provides negatively charged 2D nanoconfined channels, and rGO offers a negatively charged environment with high ion concentrations. By combining diffusion potential (E_{diff}) with redox potential (E_{redox}), the device achieves rapid Li^+ migration and electron transport under humidity activation, with a volumetric energy density of 9.46 Wh cm^{-3} and a maximum power density of 15900 W m^{-2}. This work significantly shortens the ion transport distance through a vertical design, reducing internal resistance, and combines chem-osmotic coupling with nanoconfined dynamics, offering a new solution for high-performance, high power density solid state portable osmotic power source. Moreover, Peng *et al* [115] proposed a paper-based chem-osmotic coupling system with nanoconfined channels, overcoming the inherent self-discharge defects of most batteries. This work directly integrates the chem-osmotic coupling osmotic power source onto a paper-based platform using the printing technique, providing a novel energy solution for low-cost, eco-friendly, and flexible wearable and disposable electronic devices, holding significant application potential in the fields of the Internet of Things (IoT) and biosensing.

Furthermore, therm-osmotic coupling also has been widely studied. For example, Zuo *et al* [120] investigated a therm-osmotic coupling NRED system based on COF membranes, enabling efficient osmotic power generation by simultaneously harnessing low-grade heat (<100 °C) and salinity gradients (figure 9(d)). The introduction of negatively charged sulfonate groups into the pores enhanced the surface charge density. Combined with the sub-nanoscale charged pore size (1.4–1.8 nm) of the COF membrane, the overlapping EDL within the pores significantly reduced the anion migration and improved cation selectivity. Thermal-osmotic coupling, driven by the temperature gradient (from low to high temperature), further enhanced ion dynamics. Under simulated estuarine conditions (0.01 M/0.5 M NaCl), the power density increased from 97 W m^{-2} to 231 W m^{-2} (with a 60 K temperature gradient), greatly surpassing the commercial membrane standard (5 W m^{-2}). This work achieved the synergistic utilization of both thermal and salinity gradients through surface charge density and pore design optimization, providing an efficient solution for large-scale sustainable energy harvesting and showcasing its broad potential in high-performance therm-osmotic coupling NRED system. Additionally, Zhu *et al* [79] proposed another therm-osmotic coupling system that combines thermoelectric conversion with NRED to alleviate the ICP effect and enhance energy output performance (figure 9(e)). This system used COF membranes with varying orange structures, achieving high surface charge density through functional modifications. A temperature gradient (∼40 K) was applied to the membrane to establish thermal-osmotic coupling, where the thermal gradient increases the thermophoretic mobility of ions, thereby reducing the boundary layer to alleviate ICP, effectively decreasing the ion-transport resistance, and enhancing transmembrane current. Ultimately, this osmotic power source achieved a maximum power density of 247 W m^{-2} under a 0.5 M/0.01 M NaCl gradient, offering an efficient new strategy for waste heat recovery and mitigating the ICP effect (figure 9(f)).

Besides, the introduction of light can significantly enhance ion transport dynamics. For example, Graf *et al* [125] constructed a light-osmotic coupling system based on monolayer MoS_2 nanopores, significantly improving ion selectivity and osmotic power generation performance through light-induced surface charge changes. The light-osmotic coupling was achieved by light illumination (red light at 643 nm and blue light at 475 nm) on the MoS_2 nanopore surface, triggering strong photogating effects allowing significant modulation of the charge carrier density (figure 9(g)). Illumination increases the surface charge density of the MoS_2 nanopores, enhancing ion selectivity and surface conductivity, thereby improving directional ion transport efficiency. Experimental results show that light-osmotic coupling can increase osmotic power by 131% in small pores (3 nm) and by 19% in larger pores (10 nm). This work leverages light to control surface charge and improve osmotic power output efficiency, providing a novel strategy for light-osmotic coupling to achieve efficient clean energy conversion. Xian *et al* [121] proposed a light-osmotic coupling system based on COF membranes to enhance osmotic power generation efficiency. The light-osmotic coupling was achieved by photoactive porphyrin-based COF membrane, which induces an internal electric field to accelerate ion transport (figure 6(h)). Light excites the ground-state electrons, leading to the establishment of a membrane potential between the illuminated and unilluminated sides. Experiments showed that the system achieved a maximum power density of 69.6 W m^{-2} under 50-fold NaCl salinity gradient, which represents an approximately 30% increase compared to conditions without light illumination. As shown in figure 6(i), when the light intensity increased from 40 mW cm^{-2} to 200 mW cm^{-2}, the power output significantly increased, demonstrating the synergistic enhancement of ion transport by light-osmotic coupling. This work significantly improves energy conversion performance through light-osmotic coupling, opening new research directions for low-energy, high-efficiency blue energy technologies. Moreover, Peng *et al* [115] introduced light-osmotic iontronics that leverages controlled different ion transport in nanoconfined channels and meticulously designed photochemical redox reactions to send high-throughput iontronic signals.

Additionally, Ouyang *et al* [132] proposed a light-osmotic mechanism under ultraviolet irradiation, achieved opto-iontronic current coupling within 2D nanofluidic channels of GO. This work provides valuable insights into the control of ion–electron coupling interfaces through light manipulation, enabling continuous ion current generation to counteract opposing electron displacement currents and achieve ionic rectification.

In addition to the commonly used external fields to enhance ion transport dynamics, other external factors have also been applied to address the trade-off between selectivity and permeability in IEMs. For example, Lin *et al* [126] proposed a pH-osmotic coupling system based on multifunctional polycage membranes, which achieved excellent osmotic power generation performance through pH-tunable porosity and surface charge responsiveness. The pH-osmotic coupling was realized by converting a neutral amine-functionalized cage (N-cage) into a positively charged protonated cage (A-cage) in an acidic environment, which simultaneously expands the pore size of the membrane from 4.0 Å to 6.0 Å and increases the surface positive charge density. The positive charge enhances anion selectivity, while the tunable pore structure promotes directional ion migration, effectively mitigating ICP. Experimental results showed that under simulated salinity gradient conditions (0.5 M/0.01 M NaCl), the maximum power density of the A-cage membrane increased from 1.3 W m^{-2} for N-cage to 5.8 W m^{-2}, and it achieved a power density of 22.8 W m^{-2} under Dead Sea/river water systems. This work achieves efficient, responsive osmotic power generation by simultaneously tuning the membrane's porosity and charge properties, providing an important new strategy for developing smart, tunable membrane materials. Additionally, Lai *et al* [129] proposed an ion-regulated osmotic effect based on COF-TAPB-BTDA membranes for efficient osmotic power generation. This system establishes stable ion–dipole interactions by aligned benzothiadiazole units in the nanopores of the COF membrane. This unique configuration facilitates ion–dipole interactions, allowing the for adjustable membrane surface charge in terms of polarity and intensity upon interaction with various ions, thereby providing customizable ionic transport properties (figure 9(k)). The mechanism enhancing ion transport lies in the optimized ion sieving induced by the orientation of the dipoles. Under a 0.5 M and 0.01 M NaCl salinity gradient, the membrane achieved a power density of 155 W m^{-2}, with an energy conversion efficiency of 46.1%. This work introduces the concept of aligned dipolar molecules in porous membranes, enabling dynamic ion selectivity through tunable surface charge, and providing a novel approach for biomimetic ion channels and the impact of ionic signals on the osmotic effect. Furthermore, Zhang *et al* [130] proposed a mechanical force-driven ion transport and osmotic effect system based on H_2TPP-COF monolayer membranes, enabling dynamic regulation of ion transport behavior (figure 9(l)). Under the influence of external mechanical force, the conductivity decreased anomalously, which contrasts with the increase in conductivity typically observed in low-permeable nanopores or channels dominated by capacitive effects. Through simulations, the authors discovered a unique electrical-mechanical interplay mechanism, which depends on the relative rates of ion diffusion from the boundary layer to the membrane surface and ion transport through the membrane. The high porosity of the COF monolayer membrane reduces charge accumulation caused by capacitive effects, leading to fewer ions accumulating near the membrane surface. And the high permeability of the membrane significantly accelerates the dissipation of accumulated ions under mechanical pressure, weakening the influence of the capacitive layer (CL) on the flow current. As a result, compared to low-permeability nanopores or channels, ion aggregation occurs at the electrodes rather than in the CL, dominating the flow current and producing a unique electrical-mechanical interaction mechanism. This work provides new insights into the enhancement of ion dynamics by the introduction of mechanical filed in osmotic effect systems, offering a novel perspective on the role of mechanical forces in improving ion transport behavior.

4. Conclusion and perspectives

Osmotic power generation is a promising frontier technology in the renewable energy sector that leverages the vast and sustainable salinity gradient between seawater and freshwater. The core advancement and optimization of this technology lie in the development of nanofluidic membranes, which mediate ion transport and thus dictate the efficiency of the energy conversion process. This review systematically overviewed the complex trade-off between selectivity and permeability in nanofluidic membranes of NRED systems, elucidating how these two key factors impact the overall feasibility and scalability of osmotic power systems. In particular, ICP effect plays a critical role in nanofluidic membranes, affecting both ion transport through the membrane and the overall energy conversion efficiency. By systematically exploring the fundamental mechanisms and strategies to optimize parameters, we highlight the multifaceted challenges and opportunities in optimizing current nanofluidic membranes. Furthermore, the integration of interdisciplinary approaches such as materials science, nanotechnology, and electrochemistry has been shown to be crucial in overcoming inherent trade-off and advancing the practical application of osmotic

power generation. As a perspective, several future research directions for advanced nanofluidic membrane designs to maximize the output osmotic power are outlined.

(1) Pore size is a critical parameter governing both selectivity and permeability in nanofluidic membranes. Sub-nanoscale charged pores induce significant EDL overlap, effectively repelling co-ions while facilitating counter-ion transport, thereby enhancing ion selectivity. However, excessively small pores increase membrane resistance, diminishing ion flux and power output. Conversely, larger pores improve permeability but compromise selectivity. To preserve selectivity, asymmetric structures with elevated surface charge densities are essential. Thus, optimal pore design requires a precise balance to maximize power density without significantly sacrificing selectivity or permeability. Moreover, in existing studies, achieving uniform pore shape and size remains a challenge. It is crucial to realize high uniformity and precise control over pore size to ensure consistent membrane performance and optimize its efficiency in energy conversion. Meanwhile, it is imperative to investigate the real-time aperture modulation capabilities of dynamic responsive materials (e.g. thermosensitive/photosensitive materials) to achieve optimal output performance under varying conditions.
(2) Regarding pore density, although a higher pore density might intuitively appear to enhance power output, it introduces complexities by exacerbating the ICP effect. Elevated pore density can disrupt the local salinity gradient near the membrane surface, diminishing the driving force for ion transport and impairing overall selectivity. Furthermore, intensified interactions between pores may result in a nonlinear decline in membrane conductivity, counteracting the anticipated advantages of increased pore density. Innovative strategies, such as utilizing nanoscale pore–pore coupling effects with optimized spacing, have shown promise in alleviating ICP. Framework materials like MOF, COF, and HOF offer great potential in addressing this issue.
(3) Surface charge density within nanochannels: It is another crucial factor that governs ion transport. A high surface charge density improves ion selectivity by intensifying electrostatic interactions with target ions. However, excessively high charge densities can exacerbate the ICP effect, weaken the salinity gradient, and diminish overall membrane performance, suggesting the presence of an optimal charge density range for maximizing efficiency. Additionally, introducing space charge through charged nanofibers can generate synergistic effects, highlighting the importance of fine charge management in membrane design. However, in most existing studies, charge density is influenced by pH factors. Therefore, developing nanofluidic membranes that are suitable for extreme environments (strongly acidic or alkaline conditions) is critical for the practical application of NRED systems. Furthermore, precise engineering of IEMs with spatially modulated charge density distributions along the transport channels represents a cutting-edge research direction in this field. When designing and regulating the functional groups, it is crucial to leverage their differential binding affinities toward various ions to achieve selective ion sieving effects. This approach is particularly relevant for practical applications, as it enables the membrane system to effectively handle the complex multi-ionic composition characteristic of real-world seawater and river water environments.
(4) Membrane thickness: Theoretical studies have identified that a state-of-the art option is to prepare an ultrathin membrane with a thickness of less than 1 μm, a trade-off between selectivity and permeability can be achieved, maximizing power density. However, reducing the membrane thickness does not always lead to improved performance. Ultrathin membranes may exacerbate the ICP effect, reducing power output. Conversely, excessively thick membranes increase resistance, limiting ion flux. Meanwhile, the fabrication processes of ultrathin membranes, along with their mechanical properties, require further investigation to ensure their reliability and long-term stability in practical applications. In response, a comprehensive theoretical simulation-based approach can be employed to analyze the spatial stress distribution within membranes under operational conditions. This analysis enables the strategic design of IEMs with non-uniform thickness profiles optimized according to their specific stress distribution patterns. Such an engineered design approach effectively integrates mechanical durability with enhanced power density output, addressing the trade-off between structural integrity and electrochemical performance.
(5) Ion transport pathways in nanofluidic membranes are significantly influenced by the membrane structure. Traditional vertical ion transport often results in extended high-resistance pathways, impeding ion flux. Alternative designs, such as horizontally aligned ion channels and synergistic 1D/2D synergetic transport mechanisms, have shown enhanced ion flux without compromising selectivity. Furthermore, the ordered pore structures and directionally arranged nanochannels provided by framework materials further facilitate efficient ion transport, highlighting the critical role of path optimization in achieving high-performance membranes. In the future, the development of new

materials and biomimetic membrane structures will enable the realization of ion transport pathways with higher ion flux and selectivity.

(6) Janus structure membrane: It typically composed of two parts with distinct chemical properties and physical characteristics, are renowned for their asymmetry in ion transport direction, also known as IDM. The membrane offers an effective strategy to enhance both selectivity and permeability in ion transport. By integrating different charge polarities and pore geometries within a single membrane, Janus structure enables directional ion transport, enhance ion rectification effect, and reduce ICP, resulting in high power density. Existing Janus membranes primarily focus on charge polarity structures, which alleviate ICP by expelling ions toward the bulk region in low-concentration side. However, Janus structure membranes with the same charge polarity but different charge densities, akin to biological channels, have yet to be investigated. Furthermore, to facilitate interfacial transport, it is crucial to develop heterogeneous Janus structure membrane with significantly reduced interfacial resistance. Additionally, the sub-nanoscale Janus structure membrane, composed of two continuous and defect-free thin films with ordered and aligned pore structures, has yet to be reported. Designing such membranes will help mimic biological channels with high ion selectivity and permeability, and provide deeper insights into ion transport at sub-nanoscale.

(7) External fields such as chemical, thermal, light, pH, ionic, and mechanical factors provide additional mechanisms to enhance ion transport dynamics. Coupling osmotic effect with these external fields can amplify ion flux and mitigate the ICP effect, improving both selectivity and permeability. For example, chemical and thermal-osmotic coupling effectively drives ion transport by leveraging additional energy gradients, while light-induced surface charge modulation enables dynamic control of membrane performance. The synergy between these osmotic effects and external fields opens new pathways for optimizing membrane performance and advancing the practical application of NRED systems. Additionally, the effects of other external fields, such as magnetic and acoustic fields, on ion transport and their coupling with osmotic effects remain underexplored, and the synergistic effects of multi-field coupling warrant further investigation.

(8) Despite significant progress, the scalability of nanofluidic membranes remains a major challenge. Precise micro-nano fabrication technologies developed at the laboratory scale often encounter difficulties when applied to industrial settings, especially at the coupon-scale. In addition to the previously investigated design parameters of IEMs, future research should focus on developing advanced membranes with enhanced multi-ion selectivity to address the complex ionic interference issues inherent in real-world seawater and river water systems. Typical natural water environments contain diverse ionic species (e.g. Na^+, Cl^-, Ca^{2+}, Mg^{2+}, SO_4^{2-}), whose competitive transport and mutual interactions significantly impact membrane performance. Osmotic power generation fundamentally relies on the directional migration of high-concentration ions (particularly Na^+, Cl^-) from seawater to low-concentration river water solutions. However, insufficient ion selectivity in membrane design can lead to detrimental phenomena such as 'counter-ion leakage' or 'co-ion permeation,' generating reverse currents and reducing net power output. Furthermore, issues such as membrane fouling, structural integrity under operational stresses, and long-term stability under varying environmental conditions must be addressed. Innovative fabrication methods, robust material selection, and the development of anti-fouling and self-healing membrane surfaces are key areas of ongoing research aimed at overcoming these barriers to ensure the practical feasibility of NRED systems. In this regard, the development of an *in situ* mechano-electrochemical coupling test platform is highly recommended, which would enable real-time monitoring of membrane performance degradation metrics, particularly focusing on pore size variation and charge density reduction under applied mechanical stress. Such an advanced analytical system would provide critical insights into the structural evolution and functional degradation mechanisms of IEMs during operation. Furthermore, integrating nanofluidic membranes into real-world osmotic power generation systems requires consideration of modular membrane design and system-level optimization. Membrane modules should be designed with good encapsulation and ease of maintenance to meet the needs of various scales and types of power generation systems. At the same time, ensuring consistency and repeatability of membrane performance during large-scale production is a critical challenge. Even small fabrication errors can lead to fluctuations in parameters such as pore size, pore density, and surface charge, which in turn affect membrane selectivity and permeability. Therefore, appropriate fabrication processes and optimization of process parameters are crucial. Future research should focus on multifaceted technological innovations and optimization strategies to enable the scalable and stable application of nanofluidic membranes, positioning osmotic power generation as a key component of sustainable energy solutions.

Data availability statement

All data that support the findings of this study are included within the article (and any supplementary files).

Acknowledgment

This work was supported by the National Natural Science Foundation (Grant Number 22479016). Part of the schematic diagrams for this work were created by BioRender.

ORCID iDs

Han Qian 0009-0005-8692-2317
Puguang Peng 0000-0003-3709-7101
Zhong Lin Wang 0000-0002-5530-0380
Di Wei 0000-0003-2670-6362

References

[1] Semieniuk G, Taylor L, Rezai A and Foley D K 2021 Plausible energy demand patterns in a growing global economy with climate policy *Nat. Clim. Change* **11** 313–8
[2] Schulze K, Kullmann F, Weinand J M and Stolten D 2024 Overcoming the challenges of assessing the global raw material demand of future energy systems *Joule* **8** 1936–57
[3] Logan B E and Elimelech M 2012 Membrane-based processes for sustainable power generation using water *Nature* **488** 313–9
[4] Xiao K, Jiang L and Antonietti M 2019 Ion transport in nanofluidic devices for energy harvesting *Joule* **3** 2364–80
[5] Zhou Y and Jiang L 2020 Bioinspired nanoporous membrane for salinity gradient energy harvesting *Joule* **4** 2244–8
[6] Ma X, Neek-Amal M and Sun C 2024 Advances in two-dimensional ion-selective membranes: bridging nanoscale insights to industrial-scale salinity gradient energy harvesting *ACS Nano* **18** 12610–38
[7] Zhang Z, Wen L and Jiang L 2021 Nanofluidics for osmotic energy conversion *Nat. Rev. Mater.* **6** 622–39
[8] Park H B, Kamcev J, Robeson L M, Elimelech M and Freeman B D 2017 Maximizing the right stuff: the trade-off between membrane permeability and selectivity *Science* **356** eaab0530
[9] Chu C-W, Fauziah A R and Yeh L-H 2023 Optimizing membranes for osmotic power generation *Angew. Chem., Int. Ed.* **62** e202303582
[10] Macha M, Marion S, Nandigana V V R and Radenovic A 2019 2D materials as an emerging platform for nanopore-based power generation *Nat. Rev. Mater.* **4** 588–605
[11] Allen J F 2002 Photosynthesis of ATP—electrons, proton pumps, rotors, and poise *Cell* **110** 273–6
[12] Pusch M and Zifarelli G 2015 ClC-5: physiological role and biophysical mechanisms *Cell Calcium* **58** 57–66
[13] Khakh B S, Bao X R, Labarca C and Lester H A 1999 Neuronal P2X transmitter-gated cation channels change their ion selectivity in seconds *Nat. Neurosci.* **2** 322–30
[14] The Nature Reviews Drug Discovery Ion Channel Questionnaire Participants 2004 The state of ion channel research in 2004 *Nat. Rev. Drug Discovery* **3** 239–78
[15] Doyle D A, Cabral J M, Pfuetzner R A, Kuo A, Gulbis J M, Cohen S L, Chait B T and MacKinnon R 1998 The structure of the potassium channel: molecular basis of K^+ conduction and selectivity *Science* **280** 69–77
[16] Lei D, Zhang Z and Jiang L 2024 Bioinspired 2D nanofluidic membranes for energy applications *Chem. Soc. Rev.* **53** 2300–25
[17] Tunuguntla R H, Henley R Y, Yao Y-C, Pham T A, Wanunu M and Noy A 2017 Enhanced water permeability and tunable ion selectivity in subnanometer carbon nanotube porins *Science* **357** 792–6
[18] Sheng F, Wu B, Li X, Xu T, Shehzad M A, Wang X, Ge L, Wang H and Xu T 2021 Efficient ion sieving in covalent organic framework membranes with sub-2-nanometer channels *Adv. Mater.* **33** 2104404
[19] Li S, Wang J, Lv Y, Cui Z and Wang L 2024 Nanomaterials-based nanochannel membrane for osmotic energy harvesting *Adv. Funct. Mater.* **34** 2308176
[20] Wang P, Tao W, Zhou T, Wang J, Zhao C, Zhou G and Yamauchi Y 2024 Nanoarchitectonics in advanced membranes for enhanced osmotic energy harvesting *Adv. Mater.* **36** 2404418
[21] Zhan H, Xiong Z, Cheng C, Liang Q, Liu J Z and Li D 2020 Solvation-involved nanoionics: new opportunities from 2D nanomaterial laminar membranes *Adv. Mater.* **32** 1904562
[22] Zhang Z, Huang X, Qian Y, Chen W, Wen L and Jiang L 2020 Engineering smart nanofluidic systems for artificial ion channels and ion pumps: from single-pore to multichannel membranes *Adv. Mater.* **32** 1904351
[23] Emmerich T, Ronceray N, Agrawal K V, Garaj S, Kumar M, Noy A and Radenovic A 2024 Nanofluidics *Nat. Rev. Methods Primers* **4** 69
[24] Yang L, Li S, Qian H, Wang Z, Wang Z L and Wei D 2024 Osmotic power generation based on nanoconfined materials *MRS Energy Sustain.* **11** 193–218
[25] Peng P *et al* 2024 Bioinspired ionic control for energy and information flow *Int. J. Smart Nano Mater.* **15** 1–24
[26] Peng P *et al* 2024 Photochemical iontronics with multitype ionic signal transmission at single pixel for self-driven color and tridimensional vision *Device* **3** 100574
[27] Zhang J, Liu W, Dai J and Xiao K 2022 Nanoionics from biological to artificial systems: an alternative beyond nanoelectronics *Adv. Sci.* **9** 2200534
[28] Qian H, Wei D and Wang Z 2023 Bionic iontronics based on nano-confined structures *Nano Res.* **16** 11718–30
[29] Wei D 2015 Writable electrochemical energy source based on graphene oxide *Sci. Rep.* **5** 15173
[30] Gao J, Feng Y, Guo W and Jiang L 2017 Nanofluidics in two-dimensional layered materials: inspirations from nature *Chem. Soc. Rev.* **46** 5400–24
[31] Aluru N R *et al* 2023 Fluids and electrolytes under confinement in single-digit nanopores *Chem. Rev.* **123** 2737–831

[32] Siria A, Poncharal P, Biance A-L, Fulcrand R, Blase X, Purcell S T and Bocquet L 2013 Giant osmotic energy conversion measured in a single transmembrane boron nitride nanotube *Nature* **494** 455–8
[33] Feng J, Graf M, Liu K, Ovchinnikov D, Dumcenco D, Heiranian M, Nandigana V, Aluru N R, Kis A and Radenovic A 2016 Single-layer MoS_2 nanopores as nanopower generators *Nature* **536** 197–200
[34] Liu Q, Wang Q, Qu Z and Zhang J 2023 Interfacial binding rope theory of ion transport in sub-nanochannels and its application for osmotic energy conversion *Nano Energy* **113** 108545
[35] Zhang S, Shen L, Deng H, Liu Q, You X, Yuan J, Jiang Z and Zhang S 2022 Ultrathin membranes for separations: a new era driven by advanced nanotechnology *Adv. Mater.* **34** 2108457
[36] Poroca D R, Pelis R M and Chappe V M 2017 ClC channels and transporters: structure, physiological functions, and implications in human chloride channelopathies *Front. Pharmacol.* **8** 151
[37] Hardy W B 1918 The conduction of the nervous impulse *Nature* **101** 163
[38] Hill A V 1933 The physical nature of the nerve impulse* *Nature* **131** 501–8
[39] Frankenhaeuser B 1964 Nervous impulse *Nature* **204** 1238
[40] Landowne D 1973 Movement of sodium ions associated with the nerve impulse *Nature* **242** 457–9
[41] Emperador-Melero J, Andersen J W, Metzbower S R, Levy A D, Dharmasri P A, de Nola G, Blanpied T A and Kaeser P S 2024 Distinct active zone protein machineries mediate Ca^{2+} channel clustering and vesicle priming at hippocampal synapses *Nat. Neurosci.* **27** 1680–94
[42] Hirabayashi Y *et al* 2017 ER-mitochondria tethering by PDZD8 regulates Ca^{2+} dynamics in mammalian neurons *Science* **358** 623–30
[43] Sun J, Pang Z P, Qin D, Fahim A T, Adachi R and Südhof T C 2007 A dual-Ca^{2+}-sensor model for neurotransmitter release in a central synapse *Nature* **450** 676–82
[44] Müller W and Connor J A 1991 Dendritic spines as individual neuronal compartments for synaptic Ca^{2+} responses *Nature* **354** 73–76
[45] Chance B and Mela L 1966 Proton movements in mitochondrial membranes *Nature* **212** 372–6
[46] Wikstrom M K F 1977 Proton pump coupled to cytochrome c oxidase in mitochondria *Nature* **266** 271–3
[47] Payandeh J, Scheuer T, Zheng N and Catterall W A 2011 The crystal structure of a voltage-gated sodium channel *Nature* **475** 353–8
[48] Xu L, Ding X, Wang T, Mou S, Sun H and Hou T 2019 Voltage-gated sodium channels: structures, functions, and molecular modeling *Drug. Discovery Today* **24** 1389–97
[49] Favre I, Moczydlowski E and Schild L 1996 On the structural basis for ionic selectivity among Na^+, K^+, and Ca^{2+} in the voltage-gated sodium channel *Biophys. J.* **71** 3110–25
[50] Peng P, Yang F, Li X, Li S, Wang Z and Wei D 2024 High-power iontronics enabled by nanoconfined ion dynamics *Cell Rep. Phys. Sci.* **5** 101824
[51] Cao L, Guo W, Ma W, Wang L, Xia F, Wang S, Wang Y, Jiang L and Zhu D 2011 Towards understanding the nanofluidic reverse electrodialysis system: well matched charge selectivity and ionic composition *Energy Environ. Sci.* **4** 2259–66
[52] Rollings R C, Kuan A T and Golovchenko J A 2016 Ion selectivity of graphene nanopores *Nat. Commun.* **7** 11408
[53] Xie K, Fu Q, Kim J, Lu H, He Y, Zhao Q, Scofield J, Webley P A and Qiao G G 2017 Increasing both selectivity and permeability of mixed-matrix membranes: sealing the external surface of porous MOF nanoparticles *J. Membr. Sci.* **535** 350–6
[54] Tian H, Wang Y, Pei Y and Crittenden J C 2020 Unique applications and improvements of reverse electrodialysis: a review and outlook *Appl. Energy* **262** 114482
[55] Lin S, Xu L, Chi Wang A and Wang Z L 2020 Quantifying electron-transfer in liquid-solid contact electrification and the formation of electric double-layer *Nat. Commun.* **11** 399
[56] van den Berg A, Craighead H G and Yang P 2010 From microfluidic applications to nanofluidic phenomena *Chem. Soc. Rev.* **39** 899–900
[57] Duan C and Majumdar A 2010 Anomalous ion transport in 2-nm hydrophilic nanochannels *Nat. Nanotechnol.* **5** 848–52
[58] Długołęcki P, Ogonowski P, Metz S J, Saakes M, Nijmeijer K and Wessling M 2010 On the resistances of membrane, diffusion boundary layer and double layer in ion exchange membrane transport *J. Membr. Sci.* **349** 369–79
[59] Gao J, Liu X, Jiang Y, Ding L, Jiang L and Guo W 2019 Understanding the giant gap between single-pore- and membrane-based nanofluidic osmotic power generators *Small* **15** 1804279
[60] Kim S *et al* 2023 Extreme ion-transport inorganic 2D membranes for nanofluidic applications *Adv. Mater.* **35** 2206354
[61] Wang L, Wang Z, Patel S K, Lin S and Elimelech M 2021 Nanopore-based power generation from salinity gradient: why it is not viable *ACS Nano* **15** 4093–107
[62] Tong X, Liu S, Crittenden J and Chen Y 2021 Nanofluidic membranes to address the challenges of salinity gradient power harvesting *ACS Nano* **15** 5838–60
[63] Shen J, Liu G, Han Y and Jin W 2021 Artificial channels for confined mass transport at the sub-nanometre scale *Nat. Rev. Mater.* **6** 294–312
[64] Wei R, Liu X, Cao L, Chen C, Chen I-C, Li Z, Miao J and Lai Z 2024 Zeolite membrane with sub-nanofluidic channels for superior blue energy harvesting *Nat. Commun.* **15** 10489
[65] Wang J *et al* 2024 Unlocking osmotic energy harvesting potential in challenging real-world hypersaline environments through vermiculite-based hetero-nanochannels *Nat. Commun.* **15** 608
[66] Abu-Rjal R and Green Y 2021 Bipolar nanochannels: a systematic approach to asymmetric problems *ACS Appl. Mater. Interfaces* **13** 27622–34
[67] Zhang F, Yu J, Si Y and Ding B 2023 Meta-aerogel ion motor for nanofluid osmotic energy harvesting *Adv. Mater.* **35** 2302511
[68] Gao M, Tsai P-C, Su Y-S, Peng P-H and Yeh L-H 2020 Single mesopores with high surface charges as ultrahigh performance osmotic power generators *Small* **16** 2006013
[69] Cao L X, Wen Q, Feng Y, Ji D, Li H, Li N, Jiang L and Guo W 2018 On the origin of ion selectivity in ultrathin nanopores: insights for membrane-scale osmotic energy conversion *Adv. Funct. Mater.* **28** 1804189
[70] Laucirica G, Albesa A G, Toimil-Molares M E, Trautmann C, Marmisollé W A and Azzaroni O 2020 Shape matters: enhanced osmotic energy harvesting in bullet-shaped nanochannels *Nano Energy* **71** 104612
[71] Shoemaker B A, Khalifa O and Haji-Akbari A 2024 Correlations in charged multipore systems: implications for enhancing selectivity and permeability in nanoporous membranes *ACS Nano* **18** 1420–31
[72] Lin C-Y, Chang S-F, Kuo K-T, Garner S, Pollard S C, Chen S-H and Hsu J-P 2023 Essence of the giant reduction of power density in osmotic energy conversion in porous membranes: importance of testing area *ACS Appl. Mater. Interfaces* **15** 43094–101

[73] Yang J, Tu B, Fang M, Li L and Tang Z 2022 Nanoscale pore–pore coupling effect on ion transport through ordered porous monolayers *ACS Nano* **16** 13294–300
[74] Xiao F, Ji D, Li H, Tang J, Feng Y, Ding L, Cao L, Li N, Jiang L and Guo W 2018 A general strategy to simulate osmotic energy conversion in multi-pore nanofluidic systems *Mater. Chem. Front.* **2** 935–41
[75] Yazda K, Bleau K, Zhang Y, Capaldi X, St-Denis T, Grutter P and Reisner W W 2021 High osmotic power generation via nanopore arrays in hybrid hexagonal boron nitride/silicon nitride membranes *Nano Lett.* **21** 4152–9
[76] Yang J *et al* 2022 Advancing osmotic power generation by covalent organic framework monolayer *Nat. Nanotechnol.* **17** 622–8
[77] Cheng B, Zhong Y, Qiu Y, Vaikuntanathan S and Park J 2023 Giant gateable osmotic power generation from a goldilocks two-dimensional polymer *J. Am. Chem. Soc.* **145** 5261–9
[78] Xian W, Zuo X, Zhu C, Guo Q, Meng Q-W, Zhu X, Wang S, Ma S and Sun Q 2022 Anomalous thermo-osmotic conversion performance of ionic covalent-organic-framework membranes in response to charge variations *Nat. Commun.* **13** 3386
[79] Zhu C, Zuo X, Xian W, Guo Q, Meng Q-W, Wang S, Ma S and Sun Q 2022 Integration of thermoelectric conversion with reverse electrodialysis for mitigating ion concentration polarization and achieving enhanced output power density *ACS Energy Lett.* **7** 2937–43
[80] Lo H-Y, Tsou T-Y and Hsu J-P 2022 Improving the osmotic energy conversion efficiency of multiple nanopores by a cross flow *J. Membr. Sci.* **644** 120075
[81] Ding L, Xiao D, Lu Z, Deng J, Wei Y, Caro J and Wang H 2020 Oppositely charged $Ti_3C_2T_x$ MXene membranes with 2D nanofluidic channels for osmotic energy harvesting *Angew. Chem., Int. Ed.* **59** 8720–6
[82] Ji J Z, Kang Q, Zhou Y, Feng Y, Chen X, Yuan J, Guo W, Wei Y and Jiang L 2017 Osmotic power generation with positively and negatively charged 2D nanofluidic membrane pairs *Adv. Funct. Mater.* **27** 1603623
[83] Zou K *et al* 2024 Turing-type nanochannel membranes with extrinsic ion transport pathways for high-efficiency osmotic energy harvesting *Nat. Commun.* **15** 10231
[84] Wang D *et al* 2024 Low-friction graphene oxide-based ion selective membrane for high-efficiency osmotic energy harvesting *Adv. Energy Mater.* **14** 2302262
[85] Hsu J-P, Su T-C, Peng P-H, Hsu S-C, Zheng M-J and Yeh L-H 2019 Unraveling the anomalous surface-charge-dependent osmotic power using a single funnel-shaped nanochannel *ACS Nano* **13** 13374–81
[86] Zhu C, Xian W, Song Y, Zuo X, Wang Y, Ma S and Sun Q 2022 Manipulating charge density in nanofluidic membranes for optimal osmotic energy production density *Adv. Funct. Mater.* **32** 2109210
[87] Zhang Z, Yang S, Zhang P, Zhang J, Chen G and Feng X 2019 Mechanically strong MXene/Kevlar nanofiber composite membranes as high-performance nanofluidic osmotic power generators *Nat. Commun.* **10** 2920
[88] Rao J, Lv Z, Yan X, Pan J, Chen G, Lü B and Peng F 2024 Nacre-inspired mechanically robust films for osmotic energy conversion *Adv. Funct. Mater.* **34** 2309869
[89] Zhu C, Liu P, Niu B, Liu Y, Xin W, Chen W, Kong X-Y, Zhang Z, Jiang L and Wen L 2021 Metallic two-dimensional MoS_2 composites as high-performance osmotic energy conversion membranes *J. Am. Chem. Soc.* **143** 1932–40
[90] Wang X, Wang Z, Xue Z, Fan Y, Yang J, Zhang Q, Yang N, Meng X, Jin Y and Liu S 2024 A subnano-confinement in robust MoS_2-based membranes for high-performance osmotic energy conversion *Energy Environ. Sci.* **17** 6225–33
[91] Ren Z, Zhang Q, Yin J, Jia P, Lu W, Yao Q, Deng M, Gao Y and Liu N 2024 Enhancing osmotic energy harvesting through supramolecular design of oxygen-functionalized MXene with biomimetic ion channels *Adv. Funct. Mater.* **34** 2404410
[92] Tang J *et al* 2024 All-natural 2D nanofluidics as highly-efficient osmotic energy generators *Nat. Commun.* **15** 3649
[93] Su Y-S, Hsu S-C, Peng P-H, Yang J-Y, Gao M and Yeh L-H 2021 Unraveling the anomalous channel-length-dependent blue energy conversion using engineered alumina nanochannels *Nano Energy* **84** 105930
[94] Chen J, Xin W, Kong X-Y, Qian Y, Zhao X, Chen W, Sun Y, Wu Y, Jiang L and Wen L 2020 Ultrathin and robust silk fibroin membrane for high-performance osmotic energy conversion *ACS Energy Lett.* **5** 742–8
[95] Cao L, Xiao F, Feng Y, Zhu W, Geng W, Yang J, Zhang X, Li N, Guo W and Jiang L 2017 Anomalous channel-length dependence in nanofluidic osmotic energy conversion *Adv. Funct. Mater.* **27** 1604302
[96] Kim S, Choi S, Lee H G, Jin D, Kim G, Kim T, Lee J S and Shim W 2021 Neuromorphic van der Waals crystals for substantial energy generation *Nat. Commun.* **12** 47
[97] Zhang H-G, Quan X, Du L, Wei G-L, Chen S, Yu H-T and Dong Y-C 2023 Electroregulation of graphene–nanofluid interactions to coenhance water permeation and ion rejection in vertical graphene membranes *Proc. Natl Acad. Sci. USA* **120** e2219098120
[98] Park H, Lee K H, Noh S H, Eom W, Huang J and Han T H 2024 Holey sheets enhance the packing and osmotic energy harvesting of graphene oxide membranes *ACS Nano* **18** 18584–91
[99] Qian H *et al* 2024 Horizontal transport in Ti_3C_2Tx MXene for highly efficient osmotic energy conversion from saline-alkali environments *Angew. Chem., Int. Ed.* **63** e202414984
[100] Man Z, Safaei J, Zhang Z, Wang Y, Zhou D, Li P, Zhang X, Jiang L and Wang G 2021 Serosa-mimetic nanoarchitecture membranes for highly efficient osmotic energy generation *J. Am. Chem. Soc.* **143** 16206–16
[101] Hong S, El-Demellawi J K, Lei Y, Liu Z, Marzooqi F A, Arafat H A and Alshareef H N 2022 Porous $Ti_3C_2T_x$ MXene membranes for highly efficient salinity gradient energy harvesting *ACS Nano* **16** 792–800
[102] Cao L, Chen I-C, Chen C, Shinde D B, Liu X, Li Z, Zhou Z, Zhang Y, Han Y and Lai Z 2022 Giant osmotic energy conversion through vertical-aligned ion-permselective nanochannels in covalent organic framework membranes *J. Am. Chem. Soc.* **144** 12400–9
[103] Chen C *et al* 2024 Phase engineering of zirconium MOFs enables efficient osmotic energy conversion: structural evolution unveiled by direct imaging *J. Am. Chem. Soc.* **146** 11855–65
[104] Zhang Z, Bhauriyal P, Sahabudeen H, Wang Z, Liu X, Hambsch M, Mannsfeld S C B, Dong R, Heine T and Feng X 2022 Cation-selective two-dimensional polyimine membranes for high-performance osmotic energy conversion *Nat. Commun.* **13** 3935
[105] Duan R, Zhou J, Ma X, Hao J, Zhao D, Teng C, Zhou Y and Jiang L 2023 High strength MXene/PBONF heterogeneous membrane with excellent ion selectivity for efficient osmotic energy conversion *Nano Lett.* **23** 11043–50
[106] Yang L, Cao L N Y, Li S, Peng P, Qian H, Amaratunga G, Yang F, Wang Z L and Wei D 2024 MOFs/MXene nano-hierarchical porous structures for efficient ion dynamics *Nano Energy* **129** 110076
[107] Tonnah R K *et al* 2023 Bioinspired angstrom-scale heterogeneous MOF-on-MOF membrane for osmotic energy harvesting *ACS Nano* **17** 12445–57
[108] Cao L, Chen I-C, Liu X, Li Z, Zhou Z and Lai Z 2022 An ionic diode covalent organic framework membrane for efficient osmotic energy conversion *ACS Nano* **16** 18910–20

[109] Zhou S, Xie L, Zhang X, Yan M, Zeng H, Liang K, Jiang L and Kong B 2023 Super-assembled multi-level asymmetric mesochannels for coupled accelerated dual-ion selective transport *Adv. Mater.* **35** 2208903
[110] Li C, Wen L, Sui X, Cheng Y, Gao L and Jiang L 2021 Large-scale, robust mushroom-shaped nanochannel array membrane for ultrahigh osmotic energy conversion *Sci. Adv.* **7** eabg2183
[111] Ding L, Zheng M, Xiao D, Zhao Z, Xue J, Zhang S, Caro J and Wang H 2022 Bioinspired $Ti_3C_2T_x$ MXene-based ionic diode membrane for high-efficient osmotic energy conversion *Angew. Chem., Int. Ed.* **61** e202206152
[112] Fauziah A R and Yeh L-H 2024 Engineered heterogenous subnanochannel membranes with a tri-continuous pore structure of large geometry gradient for massively enhanced osmotic power conversion from organic solutions *Adv. Funct. Mater.* **34** 2306834
[113] Zhu X, Hao J, Bao B, Zhou Y, Zhang H, Pang J, Jiang Z and Jiang L 2018 Unique ion rectification in hypersaline environment: a high-performance and sustainable power generator system *Sci. Adv.* **4** eaau1665
[114] Wang H *et al* 2024 *In situ* synthesized HOF ion rectification membrane with ultrahigh permselectivity for nanofluidic osmotic energy harvesting *Adv. Funct. Mater.* **35** 2412477
[115] Peng P, Yang F, Wang Z and Wei D 2023 Integratable paper-based iontronic power source for all-in-one disposable electronics *Adv. Energy Mater.* **13** 2302360
[116] Wei D, Yang F, Jiang Z and Wang Z 2022 Flexible iontronics based on 2D nanofluidic material *Nat. Commun.* **13** 4965
[117] Yang L *et al* 2021 A moisture-enabled fully printable power source inspired by electric eels *Proc. Natl Acad. Sci. USA* **118** e2023164118
[118] Yang F *et al* 2024 Vertical iontronic energy storage based on osmotic effects and electrode redox reactions *Nat. Energy* **9** 263–71
[119] Rastgar M, Moradi K, Burroughs C, Hemmati A, Hoek E and Sadrzadeh M 2023 Harvesting blue energy based on salinity and temperature gradient: challenges, solutions, and opportunities *Chem. Rev.* **123** 10156–205
[120] Zuo X, Zhu C, Xian W, Meng Q-W, Guo Q, Zhu X, Wang S, Wang Y, Ma S and Sun Q 2022 Thermo-osmotic energy conversion enabled by covalent-organic-framework membranes with record output power density *Angew. Chem., Int. Ed.* **61** e202116910
[121] Xian W *et al* 2024 Enhancing sustainable energy conversion efficiency by incorporating photoelectric responsiveness into multiporous ionic membrane *Small* **20** 2310791
[122] Zhu C, Xu L, Liu Y, Liu J, Wang J, Sun H, Lan Y-Q and Wang C 2024 Polyoxometalate-based plasmonic electron sponge membrane for nanofluidic osmotic energy conversion *Nat. Commun.* **15** 4213
[123] Wang J *et al* 2024 Light-responsive and ultrapermeable two-dimensional metal-organic framework membrane for efficient ionic energy harvesting *Nat. Commun.* **15** 2125
[124] Guo Q, Lai Z, Zuo X, Xian W, Wu S, Zheng L, Dai Z, Wang S and Sun Q 2023 Photoelectric responsive ionic channel for sustainable energy harvesting *Nat. Commun.* **14** 6702
[125] Graf M, Lihter M, Unuchek D, Sarathy A, Leburton J-P, Kis A and Radenovic A 2019 Light-enhanced blue energy generation using MoS_2 nanopores *Joule* **3** 1549–64
[126] Lin W, Cao L, Liu X, Alimi L O, Wang J, Moosa B A, Lai Z and Khashab N M 2024 A smart polycage membrane with responsive osmotic energy conversion based on synchronously switchable microporosity and chargeability *J. Am. Chem. Soc.* **146** 34528–35
[127] Cao L, Liu X, Shinde D B, Chen C, Chen I-C, Li Z, Zhou Z, Yang Z, Han Y and Lai Z 2022 Oriented two-dimensional covalent organic framework membranes with high ion flux and smart gating nanofluidic transport *Angew. Chem., Int. Ed.* **61** e202113141
[128] Ma Y, Yeh L-H, Lin C-Y, Mei L and Qian S 2015 pH-regulated ionic conductance in a nanochannel with overlapped electric double layers *Anal. Chem.* **87** 4508–14
[129] Lai Z *et al* 2024 Covalent–organic-framework membrane with aligned dipole moieties for biomimetic regulable ion transport *Adv. Funct. Mater.* **34** 2409356
[130] Zhang X *et al* 2023 Anomalous mechanical and electrical interplay in a covalent organic framework monolayer membrane *J. Am. Chem. Soc.* **145** 17786–94
[131] Li C, Liu P, Zhi Y, Zhai Y, Liu Z, Gao L and Jiang L 2023 Ultra-mechanosensitive chloride ion transport through bioinspired high-density elastomeric nanochannels *J. Am. Chem. Soc.* **145** 19098–106
[132] Ouyang Y, Li X, Li S, Peng P, Yang F, Wang Z L and Wei D 2023 Opto-iontronic coupling in triboelectric nanogenerator *Nano Energy* **116** 108796
[133] Ding Z, Gu T, Zhang R, Sun S, Wang K, Zhang H, Li J and Luo Y 2024 Plasma-oxidized 2D MXenes subnanochannel membrane for high-performance osmotic energy conversion *Carbon Energy* **6** e509
[134] Zhong J *et al* 2024 Permeability and selectivity synergistically enhanced nanofluidic membrane for osmotic energy harvesting *Carbon Energy* **6** e458
[135] Wang K, Yang H, Liao Z, Li S, Hambsch M, Fu G, Mannsfeld S C B, Sun Q and Zhang T 2023 Monolayer-assisted surface-initiated schiff-base-mediated aldol polycondensation for the synthesis of crystalline sp^2 carbon-conjugated covalent organic framework thin films *J. Am. Chem. Soc.* **145** 5203–10
[136] Xie Z, Xiang Z, Fu X, Lin Z, Jiao C, Zheng K, Yang M, Qin X and Ye D 2024 Decoupled ionic and electronic pathways for enhanced osmotic energy harvesting *ACS Energy Lett.* **9** 2092–100
[137] Li J, Li C, Dou H, Zhang X, Dai Y and Xia F 2024 PET-hydrogel heterogeneous membranes that eliminate concentration polarization for salinity gradient power generation *J. Membr. Sci.* **698** 122644
[138] He Y, Huang Z, Xie L, Zhang X, Hu X, Liang K, Jiang L, Zhou S and Kong B 2024 2D ordered mesoporous lamellar hetero-nanochannels with asymmetric wettability for controllable ion transport *Small* **20** 2306910
[139] Wang J, Wang L, Shao N, He M, Shang P, Cui Z, Liu S, Jiang N, Wang X and Wang L 2023 Heterogeneous two-dimensional lamellar $Ti_3C_2T_x$ membrane for osmotic power harvesting *Chem. Eng. J.* **452** 139531
[140] Li Z-Q, Zhu G-L, Mo R-J, Wu M-Y, Ding X-L, Huang L-Q, Wu Z-Q and Xia X-H 2023 Janus metal–organic framework membranes boosting the osmotic energy harvesting *ACS Appl. Mater. Interfaces* **15** 23922–30